

A discontinuous Galerkin approach for simulating graphene-based electron devices via the Boltzmann transport equation

Giovanni Nastasi¹ Vittorio Romano²

¹University of Enna “Kore”, Department of Engineering and Architecture
Plesso E - Cittadella Universitaria, 94100 - Enna, Italy
giovanni.nastasi@unikore.it

²University of Catania, Department of Mathematics and Computer Science
Viale A. Doria, 6, 95125 - Catania, Italy
vittorio.romano@unict.it

Abstract

Electron devices based on graphene have lately received a considerable interest; in fact, they could represent the ultimate miniaturization, since the active area is only one atom tick. However, the gapless dispersion relation of graphene at the Dirac points limits the possibility of using pristine graphene instead of traditional semiconductors in Field Effect Transistors (FET). For such a reason very accurate simulations are needed.

In [20] a graphene field effect transistor (GFET) has been proposed and simulated adopting a drift-diffusion model. Here, electron devices whose active area is made of monolayer graphene are simulated adopting as mathematical model the semiclassical Boltzmann transport equations (BTEs) in the bipolar case, coupled with the Poisson equation for the electric field. The system is solved by means of a discontinuous Galerkin (DG) approach [13, 14] with linear elements in the spatial coordinate and constant approximation for the wave-vector space, discretized with a polar mesh. The correct physical range for the distribution function is preserved with the maximum-principle-satisfying scheme introduced in [35].

The adopted method reveals very robust and possesses a good degree of accuracy, making it particularly well suited for capturing the complex charge transport dynamics inherent to graphene-based devices. The results for suspended monolayer graphene and GFET constitute benchmark solutions for a rigorous assessment of the validity of macroscopic models, such as drift-diffusion and hydrodynamic ones.

AMS subject classifications: 82D37, 82C70, 65M60, 82C80

Keywords: Boltzmann transport equation; discontinuous Galerkin method; graphene field effect transistors; charge transport

1 Introduction

Semiconductor materials are foundational to modern electronic devices, employed in all the technological applications. As the demand for more powerful yet energy-efficient technology grows, the field of semiconductor research requires to enhance device performance while simultaneously reducing energy consumption and mitigating environmental impact. The pursuit of greater miniaturization remains a central pillar of semiconductor innovation. Furthermore, the search for next-generation materials has led to the emergence of low-dimensional materials as a transformative area of study.

Graphene exists in a pristine form as a large area single atomic layer. It exhibits extraordinary electronic properties that could surpass the capabilities of traditional silicon-based components. The unique characteristics of this material, including high electron mobility and tunable bandgaps as in nanoribbons, position it as potential replacements for conventional semiconductors, paving the way for a new era of highly efficient and high-performance electronic devices [1].

A class of devices of this kind is represented by graphene field effect transistors (GFETs), see [2] for a comprehensive review. Such devices are commonly investigated using reduced one-dimensional models, often employing averaging procedures to simplify the description of the active region [3, 4]. Charge transport in such models is typically treated within the drift-diffusion framework. Full coupled drift-diffusion-Poisson simulations of GFETs have been proposed in [5, 6]. As an alternative, hydrodynamical models have been explored to capture additional transport phenomena [7, 8, 9, 10, 11], and in several studies thermal effects have also been incorporated [12].

A widely used deterministic approach able to numerically solve many different kinds of equations is the Discontinuous Galerkin (DG) method [13, 14]. In this work, we directly solve the semiclassical Boltzmann equation for electrons in graphene using a DG method [15, 16], extending previous studies performed in the spatially homogeneous case [17]. A first attempt have been presented in [18], where constant elements and an assigned potential have been adopted. Here, linear elements in the spatial coordinate and constant in the wave-vector space are used and the coupling with the Poisson equation is included. A major issue is the definition of numerical fluxes at the interface between two different elements. This problem is solved with an appropriate generalization of the numerical flux in the piece-wise constant case. The readers interested in finite-difference-based schemes are referred to [19].

Simulation of suspended and contacted monolayer graphene and a GFET show a good robustness and accuracy of the proposed scheme. The numerical results constitute benchmark solutions for a rigorous assessment of the validity of macroscopic models, such as drift-diffusion and hydrodynamic ones.

The plan of the paper is as follows. In Sec. 2 the semiclassical Boltzmann transport equation for charge transport in graphene is introduced including all the relevant electron-phonon scatterings and scattering with impurities. In Sec. 3 the simulated devices are described: specifically, a suspended contacted monolayer graphene, and a GFET similar to those in [20]. Sec. 4 is devoted to the numerical scheme while in the last section the numerical results are shown and discussed.

2 The semiclassical Boltzmann model

The semiclassical Boltzmann equation is considered as the most accurate model for charge transport in electron devices, except peculiar situations where quantum effects are relevant, e.g. in resonant tunneling diodes. In the case of two dimensional materials, and specifically in graphene, they read in the bipolar case as

$$\frac{\partial f_s}{\partial t} + \mathbf{v}_s \cdot \nabla_{\mathbf{x}} f_s - \frac{e}{\hbar} \mathbf{E} \cdot \nabla_{\mathbf{k}} f_s = Q(f_s, f_{-s}), \quad s = \pm, \quad (1)$$

where $f_s = f_s(t, \mathbf{x}, \mathbf{k})$ is the electron distribution function in the conduction band ($s = +$) or in the valence band ($s = -$) at time $t > 0$, position $\mathbf{x} \in D \subset \mathbb{R}^2$ and wave-vector $\mathbf{k} \in \mathcal{B} \subset \mathbb{R}^2$; D is the domain representing the active area of the device and \mathcal{B} is the first Brillouin zone. Indeed, \mathcal{B} is usually extended to \mathbb{R}^2 by homogenization [21]. In (1) e represents the elementary charge and \hbar is the reduced Planck constant. The group velocity \mathbf{v}_s is given by

$$\mathbf{v}_s = \frac{1}{\hbar} \nabla_{\mathbf{k}} \varepsilon_s(\mathbf{k}), \quad (2)$$

where $\varepsilon_s(\mathbf{k})$ is the dispersion relation of electrons. For pristine graphene one has $\varepsilon_s = s\hbar v_F |\mathbf{k}|$, v_F being the Fermi velocity which is a constant quantity.

The electric field $\mathbf{E} = \mathbf{E}(t, \mathbf{x}) = (E_x(t, \mathbf{x}), E_y(t, \mathbf{x}))$ is related to the electrostatic potential $\phi(t, \mathbf{x})$ by

$$\mathbf{E} = -\nabla_{\mathbf{x}} \phi,$$

with ϕ obtained by coupling eq.s (1) by the Poisson equation

$$\nabla \cdot (\epsilon \nabla_{\mathbf{x}} \phi) = h, \quad (3)$$

where ϵ is the dielectric constant and h the carrier density. Indeed, they depend on the specific geometry of the device and will be discussed in Sec. 3.

The collision term $Q(f_s, f_{-s})$ includes the scatterings between electrons and phonons in the graphene, and the scattering between electrons and impurities and phonons in the oxide substrate, if present,

$$Q(f_s, f_{-s}) = Q^{(el-ph)}(f_s, f_{-s}) + Q^{(el-sub)}(f_s, f_{-s}).$$

The term $Q^{(el-ph)}$ consists of several contributions: the interaction of electrons with acoustic, optical and K phonons of graphene. Acoustic phonon scattering (ac) occurs within the same valley and band (intra-valley and intra-band). Optical phonon scattering also takes place within the same valley (intra-valley) and can involve either longitudinal optical (LO) or transverse optical (TO) phonons. It may be intra-band, where the electron remains in the same energy band, or inter-band, where the electron transitions to a different band. Scattering with optical phonons of type K results in inter-valley transitions, moving electrons between adjacent valleys. If there is an oxide, remote optical phonon scattering, which is also intra-valley, can involve LO-sub and TO-sub phonons and may be intra-band or inter-band. Similarly, remote impurity scattering (imp) is limited to intra-valley and intra-band processes. In all cases, phonons are assumed to be in thermal equilibrium. Therefore, the general form of $Q^{(el-ph)}$ is

$$Q^{(el-ph)}(f_s, f_{-s}) = \sum_{s'} \left[\int_{\mathbb{R}^2} S_{s',s}^{(el-ph)}(\mathbf{k}', \mathbf{k}) f_{s'}(t, \mathbf{x}, \mathbf{k}') (1 - f_s(t, \mathbf{x}, \mathbf{k})) d\mathbf{k}' \right. \\ \left. - \int_{\mathbb{R}^2} S_{s,s'}^{(el-ph)}(\mathbf{k}, \mathbf{k}') f_s(t, \mathbf{x}, \mathbf{k}) (1 - f_{s'}(t, \mathbf{x}, \mathbf{k}')) d\mathbf{k}' \right],$$

where the total transition rate is given by the sum of the contributions of the several types of scatterings

$$S_{s',s}^{(el-ph)}(\mathbf{k}', \mathbf{k}) = \sum_{\nu} \left| G_{s',s}^{(\nu)}(\mathbf{k}', \mathbf{k}) \right|^2 \left[(n_{\mathbf{q}}^{(\nu)} + 1) \delta(\varepsilon_s(\mathbf{k}) - \varepsilon_{s'}(\mathbf{k}') + \hbar\omega_{\mathbf{q}}^{(\nu)}) \right. \\ \left. + n_{\mathbf{q}}^{(\nu)} \delta(\varepsilon_s(\mathbf{k}) - \varepsilon_{s'}(\mathbf{k}') - \hbar\omega_{\mathbf{q}}^{(\nu)}) \right]. \quad (4)$$

The index ν labels the ν th phonon mode, $\left| G_{s',s}^{(\nu)}(\mathbf{k}', \mathbf{k}) \right|^2$ is the matrix element, which describes the scattering mechanism, due to phonons of type ν , between electrons belonging to the band s' and electrons belonging to the band s . The symbol δ denotes the Dirac distribution, $\omega_{\mathbf{q}}^{(\nu)}$ is the the ν th phonon frequency, $n_{\mathbf{q}}^{(\nu)}$ is the Bose-Einstein distribution for the phonon of type ν

$$n_{\mathbf{q}}^{(\nu)} = \frac{1}{e^{\hbar\omega_{\mathbf{q}}^{(\nu)}/k_B T} - 1},$$

k_B being the Boltzmann constant and T being the graphene lattice temperature which, in this article, is assumed constant. When, for a phonon ν_* , $\hbar\omega_{\mathbf{q}}^{(\nu_*)} \ll k_B T$, then the scattering with the phonon ν_* can be assumed elastic. In this case, we eliminate in Eq. (4) the term $\hbar\omega_{\mathbf{q}}^{(\nu_*)}$ inside the delta distribution and we use the approximation $n_{\mathbf{q}}^{(\nu_*)} + 1 \approx n_{\mathbf{q}}^{(\nu_*)}$.

Now we write explicitly the transition rates used in our simulations. For acoustic phonons, usually one considers the elastic approximation for which the following relation holds

$$2 n_{\mathbf{q}}^{(ac)} \left| G^{(ac)}(\mathbf{k}', \mathbf{k}) \right|^2 = \frac{1}{(2\pi)^2} \frac{\pi D_{ac}^2 k_B T}{2\hbar\sigma_m v_p^2} (1 + \cos\vartheta_{\mathbf{k},\mathbf{k}'}) , \quad (5)$$

where D_{ac} is the acoustic phonon coupling constant, v_p is the sound speed in graphene, σ_m the graphene areal density, and $\vartheta_{\mathbf{k},\mathbf{k}'}$ is the convex angle between \mathbf{k} and \mathbf{k}' .

There are three relevant optical phonon scatterings: the longitudinal optical (LO), the transversal optical (TO) and the K phonons. The matrix elements read

$$\left| G^{(LO)}(\mathbf{k}', \mathbf{k}) \right|^2 + \left| G^{(TO)}(\mathbf{k}', \mathbf{k}) \right|^2 = \frac{2}{(2\pi)^2} \frac{\pi D_O^2}{\sigma_m \omega_O}, \quad (6)$$

$$\left| G^{(K)}(\mathbf{k}', \mathbf{k}) \right|^2 = \frac{1}{(2\pi)^2} \frac{2\pi D_K^2}{\sigma_m \omega_K} (1 - \cos\vartheta_{\mathbf{k},\mathbf{k}'}) . \quad (7)$$

Here D_O is the optical phonon coupling constant, ω_O the optical phonon frequency, D_K is the K-phonon coupling constant and ω_K the K-phonon frequency.

Regarding the scatterings of electrons with the substrate, the collision term $Q^{(el-sub)}$ is given by

$$S_{s',s}^{(el-sub)}(\mathbf{k}', \mathbf{k}) = S_{s',s}^{(O-sub)}(\mathbf{k}', \mathbf{k}) + S_{s',s}^{(imp)}(\mathbf{k}', \mathbf{k}),$$

with

$$S_{s',s}^{(O-sub)}(\mathbf{k}', \mathbf{k}) = \left| G^{(O-sub)}(\mathbf{k}', \mathbf{k}) \right|^2 \left[\left(n_{\mathbf{q}}^{(O-sub)} + 1 \right) \delta \left(\varepsilon_s(\mathbf{k}) - \varepsilon_{s'}(\mathbf{k}') + \hbar \omega_{\mathbf{q}}^{(O-sub)} \right) \right. \\ \left. + n_{\mathbf{q}}^{(O-sub)} \delta \left(\varepsilon_s(\mathbf{k}) - \varepsilon_{s'}(\mathbf{k}') - \hbar \omega_{\mathbf{q}}^{(O-sub)} \right) \right],$$

where

$$\left| G^{(O-sub)}(\mathbf{k}', \mathbf{k}) \right|^2 = \left| G^{(LO-sub)}(\mathbf{k}', \mathbf{k}) \right|^2 + \left| G^{(TO-sub)}(\mathbf{k}', \mathbf{k}) \right|^2 = \frac{2}{(2\pi)^2} \frac{\pi D_{O-sub}^2}{\sigma_m \omega_{O-sub}}.$$

Concerning $S^{(imp)}$, we assume that the remote impurities interacting with the charge carriers are those located in a plane within the oxide at distance d from the graphene sheet. The definition of the scattering rate for electron-impurity scattering is highly complex; so many approximate models are proposed in the literature. Following [22], we adopt the expression

$$S_{s',s}^{(imp)}(\mathbf{k}, \mathbf{k}') = \frac{2\pi}{\hbar} \frac{n_i}{(2\pi)^2} \left| \frac{V_i(|\mathbf{k} - \mathbf{k}'|, d)}{\epsilon(|\mathbf{k} - \mathbf{k}'|)} \right|^2 \frac{(1 + \cos \vartheta_{\mathbf{k}, \mathbf{k}'})}{2} \delta(\varepsilon_s(\mathbf{k}') - \varepsilon_{s'}(\mathbf{k})), \quad (8)$$

where, since the scattering is elastic, the only admissible cases are given by $s = s'$. In (8) the parameter n_i is the number of impurities per unit area while V_i is the screened Coulomb impurity potential given by

$$V_i(|\mathbf{k} - \mathbf{k}'|, d) = 2\pi e^2 \frac{\exp(-d|\mathbf{k} - \mathbf{k}'|)}{\tilde{\kappa}|\mathbf{k} - \mathbf{k}'|},$$

where $\tilde{\kappa}$ is the effective dielectric constant, defined by $4\pi\epsilon_0(\kappa_{top} + \kappa_{bottom})/2$, ϵ_0 being the vacuum dielectric constant, κ_{top} and κ_{bottom} being the relative dielectric constants of the medium above and below the graphene layer respectively. The dielectric screening function ϵ in graphene is approximated with the 2D finite temperature static random phase approximation (RPA)

$$\epsilon(|\mathbf{k} - \mathbf{k}'|) = \begin{cases} 1 + \frac{q_s}{|\mathbf{k} - \mathbf{k}'|} - \frac{\pi q_s}{8k_F}, & \text{if } |\mathbf{k} - \mathbf{k}'| < 2k_F, \\ 1 + \frac{q_s}{|\mathbf{k} - \mathbf{k}'|} - \frac{q_s \sqrt{|\mathbf{k} - \mathbf{k}'|^2 - 4k_F^2}}{2|\mathbf{k} - \mathbf{k}'|^2} - \frac{q_s}{4k_F} \arcsin \left(\frac{2k_F}{|\mathbf{k} - \mathbf{k}'|} \right), & \text{otherwise,} \end{cases}$$

where $q_s = \frac{4e^2 k_F}{\tilde{\kappa} \hbar v_F}$ is the effective Thomas-Fermi wave-vector for graphene with $k_F = \frac{\varepsilon_F}{\hbar v_F}$ the Fermi wave-vector. Observe that if $\varepsilon_F = 0$ the dielectric function is not defined. To overcome the problem, according to [23] if $|\varepsilon_F| < 0.04$ eV we adopt the approximate expression $k_F = \sqrt{\frac{4\pi n}{g_s g_v}}$, being n the 2D carrier density, $g_s = 2$ and $g_v = 2$ the spin and valley degeneracy. To simplify the computation, the constant value $\varepsilon_F = 0.25$ eV has been used.

In a situation which is spatially non homogeneous the Fermi level depends on the position but with good accuracy its value ranges around the one given by the work function at the metallic contacts. Therefore, we consider the Fermi level as a constant with the same value of the work function. See the Section 3 for further details.

We remark that there is a certain degree of uncertainty in the literature regarding the values of the parameters involved in the scattering processes. In our simulations, we use the physical parameters listed in Table 1. For further details, the reader is referred to [24]. As demonstrated in [25], the distance d plays a critical role in accurately predicting electron velocity, and consequently, electron mobility. In [26], numerical simulations were carried out for the unipolar case, treating d as a random variable. In this work we assume d to be constant. This choice is supported by the findings in [26], where the results obtained considering d a random variable were found to be practically equivalent to those using the average value of this parameter.

Once one gets the distribution functions f_s solving the equations (1), the macroscopic quantities of interests are evaluated as averages with respect to the wave-vector. Of particular interest are the carrier density $n(t, \mathbf{x})$, the current density $\mathbf{j}^n(t, \mathbf{x}) = (j^{n,x}(t, \mathbf{x}), j^{n,y}(t, \mathbf{x}))$ and the energy density $\mathcal{E}^n(t, \mathbf{x})$. For

Parameter	Value
v_F	10^8 cm/s
σ_m	7.6×10^{-8}
$\hbar\omega_O$	164.6 meV
$\hbar\omega_K$	124 meV
v_p	2×10^6 cm/s
D_{ac}	6.8 eV
D_O	10^9 eV/cm
D_K	3.5×10^8 eV/cm
$\hbar\omega_{O-sub}$ (SiO ₂)	55 meV
D_{O-sub} (SiO ₂)	5.14×10^7 eV/cm
n_i (SiO ₂)	2.5×10^{11} cm ⁻²
κ_{sub} (SiO ₂)	3.9

Table 1: Physical parameters for the electron-phonon collision term.

the electron in the conduction band they are defined as

$$\begin{aligned} n(t, \mathbf{x}) &= \frac{g_v g_s}{(2\pi)^2} \int_{\mathbb{R}^2} f_+(t, \mathbf{x}, \mathbf{k}) d\mathbf{k}, \\ \mathbf{j}^n(t, \mathbf{x}) &= -e \frac{g_v g_s}{(2\pi)^2} \int_{\mathbb{R}^2} \mathbf{v}_+(\mathbf{k}) f_+(t, \mathbf{x}, \mathbf{k}) d\mathbf{k}, \\ \mathcal{E}^n(t, \mathbf{x}) &= \frac{g_v g_s}{(2\pi)^2} \int_{\mathbb{R}^2} \varepsilon_+(\mathbf{k}) f_+(t, \mathbf{x}, \mathbf{k}) d\mathbf{k}. \end{aligned}$$

All the quantities are evaluated at time t and position \mathbf{x} . Other macroscopic quantities directly related to the ones defined above are the electron mean velocity $\mathbf{V}^n(t, \mathbf{x})$ and the electron mean energy $E^n(t, \mathbf{x})$, which are defined as

$$\begin{aligned} \mathbf{V}^n(t, \mathbf{x}) &= -\frac{1}{e} \frac{\mathbf{j}^n(t, \mathbf{x})}{n(t, \mathbf{x})}, \\ E^n(t, \mathbf{x}) &= \frac{\mathcal{E}^n(t, \mathbf{x})}{n(t, \mathbf{x})}. \end{aligned}$$

In the valence band, instead of electrons, is convenient to consider holes [21] to avoid integrability issues. It is possible to verify [17] that

$$f_h(t, \mathbf{x}, \mathbf{k}) = 1 - f_-(t, \mathbf{x}, \mathbf{k}), \quad \varepsilon_h(\mathbf{k}) = \varepsilon_+(\mathbf{k}), \quad \mathbf{v}_h(\mathbf{k}) = \mathbf{v}_+(\mathbf{k}). \quad (9)$$

where the subscript h means quantity referred to holes. Similarly to electrons, the macroscopic quantities for holes are given by

$$\begin{aligned} p(t, \mathbf{x}) &= \frac{g_v g_s}{(2\pi)^2} \int_{\mathbb{R}^2} f_h(t, \mathbf{x}, \mathbf{k}) d\mathbf{k}, \\ \mathbf{j}^p(t, \mathbf{x}) &= e \frac{g_v g_s}{(2\pi)^2} \int_{\mathbb{R}^2} \mathbf{v}_h(\mathbf{k}) f_h(t, \mathbf{x}, \mathbf{k}) d\mathbf{k}, \\ \mathcal{E}^p(t, \mathbf{x}) &= \frac{g_v g_s}{(2\pi)^2} \int_{\mathbb{R}^2} \varepsilon_h(\mathbf{k}) f_h(t, \mathbf{x}, \mathbf{k}) d\mathbf{k}, \end{aligned}$$

where $p(t, \mathbf{x})$ is the hole density, $\mathbf{j}^p(t, \mathbf{x}) = (j^{p,x}(t, \mathbf{x}), j^{p,y}(t, \mathbf{x}))$ is the current density of holes and \mathcal{E}^p the energy density of holes. The hole mean velocity $\mathbf{V}^p(t, \mathbf{x})$ and the hole mean energy $E^p(t, \mathbf{x})$ are defined as

$$\begin{aligned} \mathbf{V}^p(t, \mathbf{x}) &= \frac{1}{e} \frac{\mathbf{j}^p(t, \mathbf{x})}{p(t, \mathbf{x})}, \\ E^p(t, \mathbf{x}) &= \frac{\mathcal{E}^p(t, \mathbf{x})}{p(t, \mathbf{x})}. \end{aligned}$$

The total current density is given by

$$\mathbf{j}^{tot}(t, \mathbf{x}) = \mathbf{j}^n(t, \mathbf{x}) - \mathbf{j}^p(t, \mathbf{x}). \quad (10)$$

Regarding the existence and uniqueness of solution of the semiclassical Boltzmann equation (1), the results in [27] can be adapted.

3 Physical setting

As first test case, we consider a suspended monolayer graphene with two metallic contacts placed at the extremities, as in Fig. 1. We take the electric field a constant external field. So the BTE is not coupled with the Poisson equation.

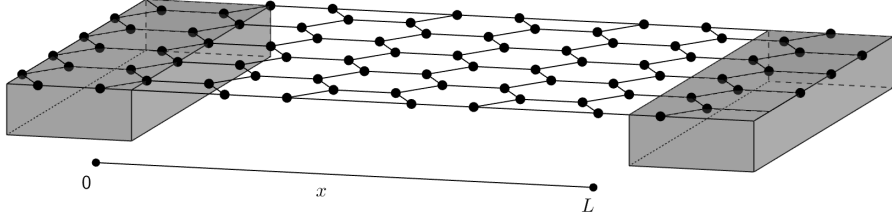


Figure 1: Contacted monolayer graphene.

It is convenient to write Eq.s (1) in terms of energy ε and angle θ , measured from the transversal direction oriented as in Fig. 1, instead of \mathbf{k} . One has

$$(k_x, k_y) = \frac{\varepsilon}{\hbar v_F} (\cos \theta, \sin \theta), \quad (11)$$

and the Jacobian of the transformation is $\varepsilon/(\hbar v_F)^2$. In this way, the group velocity reads

$$\mathbf{v}_s = s v_F \frac{\mathbf{k}}{|\mathbf{k}|} = s v_F (\cos \theta, \sin \theta). \quad (12)$$

Moreover, we have

$$\nabla_{\mathbf{k}} f_s = \hbar v_F \frac{\partial f_s}{\partial \varepsilon} \mathbf{e}_\varepsilon + \frac{\hbar v_F}{\varepsilon} \frac{\partial f_s}{\partial \theta} \mathbf{e}_\theta, \quad (13)$$

where

$$\begin{aligned} \mathbf{e}_\varepsilon &= \cos \theta \mathbf{i} + \sin \theta \mathbf{j}, \\ \mathbf{e}_\theta &= -\sin \theta \mathbf{i} + \cos \theta \mathbf{j}. \end{aligned}$$

We consider the material along the directions of the contact as infinite. Therefore the symmetry of the structure allows us to treat the problem as one dimensional. If we denote with x the abscissa in the direction orthogonal to the contacts the Boltzmann equations write

$$\frac{\partial f_s}{\partial t} + s v_F \cos \theta \frac{\partial f_s}{\partial x} - e v_F E_x \cos \theta \frac{\partial f_s}{\partial \varepsilon} + \frac{e v_F E_x}{\varepsilon} \sin \theta \frac{\partial f_s}{\partial \theta} = Q(f_s, f_{-s}), \quad (14)$$

where now $f_s = f_s(t, x, \varepsilon, \theta)$ with $t > 0$, $x \in [0, L]$, $\varepsilon \in [0, +\infty[$ and $\theta \in [0, 2\pi]$. The domain $[0, L]$, with $L > 0$, is the numerical domain representing the transversal section of the device. In order to keep the divergence form of the transport part of the equation, we multiply Eq. 14 by the Jacobian, obtaining

$$\frac{\varepsilon}{(\hbar v_F)^2} \frac{\partial f_s}{\partial t} + s \frac{v_F}{(\hbar v_F)^2} \frac{\partial}{\partial x} (\varepsilon \cos \theta f_s) - e E_x \frac{v_F}{(\hbar v_F)^2} \left[\frac{\partial}{\partial \varepsilon} (\varepsilon \cos \theta f_s) - \frac{\partial}{\partial \theta} (\sin \theta f_s) \right] = \frac{\varepsilon}{(\hbar v_F)^2} Q(f_s, f_{-s}). \quad (15)$$

As initial conditions we assign the intrinsic equilibrium distribution

$$f_s(0, x, \varepsilon, \theta) = f_{FD}^s(\varepsilon, 0), \quad \forall x \in]0, L[\quad (16)$$

where f_{FD} is the Fermi-Dirac distribution

$$f_{FD}^s(\varepsilon, \varepsilon_F) = \frac{1}{1 + \exp\left(\frac{s\varepsilon - \varepsilon_F}{k_B T}\right)}, \quad (17)$$

with ε_F Fermi level. At $x = 0$ and $x = L$ we set inflow boundary conditions

$$f_s(t, 0, \varepsilon, \theta) = f_{FD}^s(\varepsilon, \varepsilon_F), \quad \forall t > 0, \quad \forall \varepsilon \geq 0, \quad \forall \theta \in [-\pi/2, \pi/2], \quad (18)$$

$$f_s(t, L, \varepsilon, \theta) = f_{FD}^s(\varepsilon, \varepsilon_F), \quad \forall t > 0, \quad \forall \varepsilon \geq 0, \quad \forall \theta \in [\pi/2, 3/2\pi], \quad (19)$$

where ε_F takes an assigned value.

As second test case, we simulate charge transport in a field-effect transistor (FET) having the active area made of monolayer large-area graphene (GFET). We choose the geometry introduced in [20], where the same authors have performed the simulation by solving the drift-diffusion equations. The active zone, made of graphene, is placed between two strips of insulator, both of them being SiO_2 . The simulated device is depicted in Fig. 2. The source and drain metallic contacts are directly attached to the graphene. The two gate contacts (up and down) are upon the oxide.

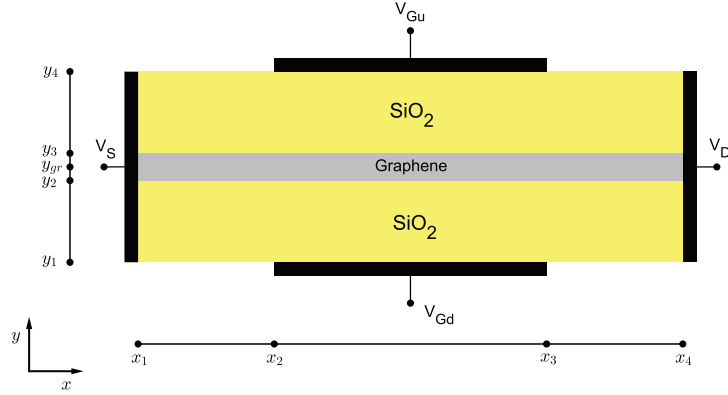


Figure 2: GFET.

The domain consists of a rectangle of length L and height H , which represents a section of the GFET, with $L = x_4 - x_1$ and $H = y_4 - y_1$. The Boltzmann equation (14) is set for $x \in [x_1, x_4]$ along $y = y_{gr}$. We fix $x_1 = y_1 = 0$. The initial condition is as in the previous case.

The boundary conditions need more explanation because modeling the metal-graphene interface is a critical challenge. The contacts are treated as thermal reservoirs, wherein charge carriers are assumed to follow a Fermi-Dirac distribution. Charge injection across the interface is governed by the difference in work functions between the contact metal and graphene, which is inherently dependent on the specific material employed for the electrodes. Copper is regarded as one of the most suitable substrates for graphene deposition via chemical vapor deposition (CVD), owing to its favorable surface properties. Notably, the interaction between copper and graphene is among the weakest observed for metallic contacts. First-principles calculations based on density functional theory (DFT) [28] predict a Fermi level shift of $\Delta\varepsilon_F = -0.275$ eV relative to the Dirac point at the Cu(111)/graphene junction, resulting in an induced n-type doping. This theoretical prediction aligns with experimental observations, which report Fermi level shifts ranging from 0.20 eV [29] to 0.30 eV [30] in absolute magnitude. For subsequent analysis, we adopt a representative value of $\Delta\varepsilon_F = -0.25$ eV corresponding to a built-in potential of $V_{built} = -\Delta\varepsilon_F/e = 0.25$ V. Therefore at $x = x_1$ and $x = x_4$ inflow boundary conditions

$$f_s(t, 0, \varepsilon, \theta) = f_{FD}^s(\varepsilon, e\phi_W), \quad \forall t > 0, \quad \forall \varepsilon \geq 0, \quad \forall \theta \in [-\pi/2, \pi/2], \quad (20)$$

$$f_s(t, L, \varepsilon, \theta) = f_{FD}^s(\varepsilon, e\phi_W), \quad \forall t > 0, \quad \forall \varepsilon \geq 0, \quad \forall \theta \in [\pi/2, 3/2\pi], \quad (21)$$

are assumed where ϕ_W is the work function of the metallic contacts. We assume they are made of copper, so $e\phi_W = 0.25$ eV.

For the complete simulation, a self consistent electric field is required solving the Poisson equation (3) coupled with the transport equation. In the specific case of the device of Fig. 2, we set

$$\epsilon(x, y) = \begin{cases} \epsilon_{gr} & \forall (x, y) \in [x_1, x_4] \times [y_2, y_3] \\ \epsilon_{ox} & \forall (x, y) \in [x_1, x_4] \times ([y_1, y_2] \cup [y_3, y_4]) \end{cases} \quad (22)$$

where $\epsilon_{gr} = 3.3\epsilon_0$ and $\epsilon_{ox} = 3.6\epsilon_0$ are the dielectric constant of graphene and oxide (SiO_2) respectively, ϵ_0 being the dielectric constant in the vacuum. The right hand side of eq. (3) writes

$$h(x, y) = \begin{cases} \frac{e(n(x) - p(x) - n_i)}{t_{gr}} & \forall (x, y) \in [x_1, x_4] \times [y_2, y_3] \\ 0 & \text{otherwise} \end{cases} \quad (23)$$

$n(x)$ and $p(x)$ represent the electron and hole density respectively, $n_i = 2.5 \cdot 10^3 \mu\text{m}^{-2}$ is the areal density of the impurity charges at the graphene/oxide interface, and $t_{gr} = 1 \text{ nm}$ is the thickness between the two strips of oxide, delimited by y_2 and y_3 . We assume the charges in graphene are distributed in such a volume. For eq. (3) we impose the following boundary conditions

$$\begin{aligned} \phi &= 0 & \forall (x, y) \in \{x_1\} \times [y_1, y_4] \\ \phi &= V_b & \forall (x, y) \in \{x_4\} \times [y_1, y_4] \\ \phi &= V_{G_d} & \forall (x, y) \in [x_2, x_3] \times \{y_1\} \\ \phi &= V_{G_u} & \forall (x, y) \in [x_2, x_3] \times \{y_4\} \\ \nabla_\nu \phi &= 0 & \text{at the remaining part of the boundary} \end{aligned} \quad (24)$$

where V_b is the bias voltage while V_{G_d} and V_{G_u} are the upper and down gate voltages.

4 Numerical method

We present the 2D case in space; the 1D case can be obtained in a straightforward way. First of all, we define a numerical mesh in space to discretize the domain $[0, L] \times [0, H]$ by $(N_x + 1) \cdot (N_y + 1)$ grid points. The vertices of each 2D cell are denoted by

$$\begin{aligned} x_{i+1/2} &= i\Delta x, & \text{for } i = 0, 1, \dots, N_x, \\ y_{j+1/2} &= j\Delta y, & \text{for } j = 0, 1, \dots, N_y, \end{aligned}$$

where $\Delta x = L/N_x$ and $\Delta y = H/N_y$. The midpoints are given by

$$\begin{aligned} x_i &= \left(i - \frac{1}{2}\right)\Delta x, & \text{for } i = 1, 2, \dots, N_x, \\ y_j &= \left(j - \frac{1}{2}\right)\Delta y, & \text{for } j = 1, 2, \dots, N_y. \end{aligned}$$

The reason for such a choice of the indices will be clear in the sequel.

We discretize the Poisson equation by standard finite differencing. For the sake of simplifying the notation, the explicit dependence on time is omitted. Letting $\phi_{i+1/2,j+1/2} \approx \phi(x_{i+1/2}, y_{j+1/2})$, for $i = 0, 1, \dots, N_x$ and $j = 0, 1, \dots, N_y$, we get

$$\begin{aligned} & \frac{\epsilon_{i+1,j+1/2}}{\Delta x^2} \phi_{i+3/2,j+1/2} - \frac{\epsilon_{i+1,j+1/2} + \epsilon_{i,j+1/2}}{\Delta x^2} \phi_{i+1/2,j+1/2} + \frac{\epsilon_{i,j+1/2}}{\Delta x^2} \phi_{i-1/2,j+1/2} \\ & + \frac{\epsilon_{i+1/2,j+1}}{\Delta y^2} \phi_{i+1/2,j+3/2} - \frac{\epsilon_{i+1/2,j+1} + \epsilon_{i+1/2,j}}{\Delta y^2} \phi_{i+1/2,j+1/2} + \frac{\epsilon_{i+1/2,j}}{\Delta y^2} \phi_{i+1/2,j-1/2} = h_{i+1/2,j+1/2}, \end{aligned} \quad (25)$$

where $\epsilon_{i,j+1/2} = \epsilon(x_i, y_{j+1/2})$ for all $i = 1, 2, \dots, N_x$, $j = 1, 2, \dots, N_y - 1$, $\epsilon_{i+1/2,j} = \epsilon(x_{i+1/2}, y_j)$ for all $i = 1, 2, \dots, N_x - 1$, $j = 1, 2, \dots, N_y$, and $h_{i+1/2,j+1/2} = h(x_{i+1/2}, y_{j+1/2})$ for all $i = 1, 2, \dots, N_x - 1$, $j = 1, 2, \dots, N_y - 1$. One gets $(N_x - 1)(N_y - 1)$ equations. Further $2(N_x + N_y)$ equations are determined by imposing the boundary conditions. We pay attention to choose N_y such that y_{gr} is a grid point.

To discretize the semiclassical Boltzmann equations in $[0, L] \times \{y_{gr}\}$ a DG method is adopted. Since we expect an exponential decay of f_+ and $1 - f_-$, as $\varepsilon \rightarrow +\infty$, it is reasonable to choose a maximum value of energy ε_{max} to make the numerical domain in energy a compact set. Overall we have partitionate the complete numerical domain in $N_x \times N_\varepsilon \times N_\theta$ open cells $C_{i,k,n}$, with N_ε and N_θ positive integer, such that

$$[0, L] \times [0, \varepsilon_{max}] \times [0, 2\pi] = \bigcup_{i=1}^{N_x} \bigcup_{k=1}^{N_\varepsilon} \bigcup_{n=1}^{N_\theta} \overline{C}_{i,k,n}$$

$\overline{C}_{i,k,n}$ being the closure of $C_{i,k,n}$. We define three sets of index

$$I_x = \{1, 2, \dots, N_x\}, \quad I_\varepsilon = \{1, 2, \dots, N_\varepsilon\}, \quad I_\theta = \{1, 2, \dots, N_\theta\}.$$

For all $(i, k, n) \in I_x \times I_\varepsilon \times I_\theta$ the cells are given by

$$C_{i,k,n} = \left[x_{i-\frac{1}{2}}, x_{i+\frac{1}{2}} \right] \times \left\{ (\varepsilon, \theta) \in [0, \varepsilon_{max}] \times [0, 2\pi] : \varepsilon_{k-\frac{1}{2}} < \varepsilon < \varepsilon_{k+\frac{1}{2}}, \theta_{n-\frac{1}{2}} < \theta < \theta_{n+\frac{1}{2}} \right\},$$

where $x_{i\pm\frac{1}{2}}$ are the same grid points of the discretization of Poisson's equation and

$$\begin{aligned} \varepsilon_{k+1/2} &= k\Delta\varepsilon, & \text{for } k = 0, 1, \dots, N_\varepsilon, \\ \theta_{n+1/2} &= n\Delta\theta, & \text{for } n = 0, 1, \dots, N_\theta, \end{aligned}$$

with $\Delta\varepsilon = \varepsilon_{max}/N_\varepsilon$ and $\Delta\theta = 2\pi/N_\theta$. The midpoints are given by

$$\begin{aligned} \varepsilon_k &= \left(k - \frac{1}{2} \right) \Delta\varepsilon, & \text{for } k = 1, 2, \dots, N_\varepsilon, \\ \theta_n &= \left(n - \frac{1}{2} \right) \Delta\theta, & \text{for } n = 1, 2, \dots, N_\theta. \end{aligned}$$

Since the energy is proportional to the modulus of the wave-vector, the adopted grid is a polar one in the \mathbf{k} -space, as shown in Fig. 3.

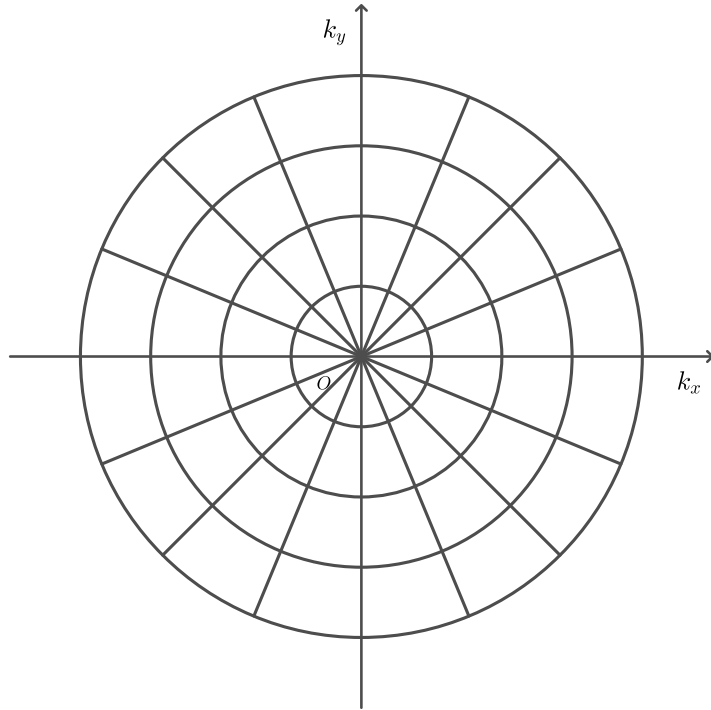


Figure 3: Polar grid in the space of wave-vectors.

We look for an approximation \tilde{f}_s of f_s such that, for each time $t \in [0, T]$, \tilde{f}_s belongs to the finite dimensional space

$$\tilde{V} = \{ v \in L^1 ([0, L] \times [0, \varepsilon_{max}] \times [0, 2\pi]) : v|_{C_{i,k,n}} \in P^{m,r,l}(C_{i,k,n}) \quad \forall (i, k, n) \in I_x \times I_\varepsilon \times I_\theta \}$$

where $P^{m,r,l}(C_{i,k,n})$ denotes the space of the polynomials defined in $C_{i,k,n}$ of degree at most m in x , at most r in ε and at most l in θ . In order to determine the approximate solution \tilde{f}_s we use a weak formulation of our problem. In each cell we multiply the equation (15) by arbitrary smooth function v

and integrate over $C_{i,k,n}$,

$$\begin{aligned} & \int_{C_{i,k,n}} v(x, \varepsilon, \theta) \left\{ \frac{\varepsilon}{(\hbar v_F)^2} \frac{\partial f_s}{\partial t} + s \frac{v_F}{(\hbar v_F)^2} \frac{\partial}{\partial x} (\varepsilon \cos \theta f_s) - e E_x \frac{v_F}{(\hbar v_F)^2} \left[\frac{\partial}{\partial \varepsilon} (\varepsilon \cos \theta f_s) - \frac{\partial}{\partial \theta} (\sin \theta f_s) \right] \right\} dx d\varepsilon d\theta \\ &= \int_{C_{i,k,n}} v(x, \varepsilon, \theta) \frac{\varepsilon}{(\hbar v_F)^2} Q(f_s, f_{-s}) dx d\varepsilon d\theta. \end{aligned} \quad (26)$$

A weak solution in the considered cell is a function that satisfies the previous relation for any test function v .

In the spirit of the DG method, we replace v with a test function $\tilde{v} \in \tilde{V}$ and f_s with the approximation \tilde{f}_s , getting in each cell the discretized weak formulation

$$\begin{aligned} & \int_{C_{i,k,n}} \tilde{v}(x, \varepsilon, \theta) \left\{ \frac{\varepsilon}{(\hbar v_F)^2} \frac{\partial \tilde{f}_s}{\partial t} + s \frac{v_F}{(\hbar v_F)^2} \frac{\partial}{\partial x} (\varepsilon \cos \theta \tilde{f}_s) - e E_x \frac{v_F}{(\hbar v_F)^2} \left[\frac{\partial}{\partial \varepsilon} (\varepsilon \cos \theta \tilde{f}_s) - \frac{\partial}{\partial \theta} (\sin \theta \tilde{f}_s) \right] \right\} dx d\varepsilon d\theta \\ &= \int_{C_{i,k,n}} \tilde{v}(x, \varepsilon, \theta) \frac{\varepsilon}{(\hbar v_F)^2} Q(\tilde{f}_s, \tilde{f}_{-s}) dx d\varepsilon d\theta \quad \forall \tilde{v} \in \tilde{V}. \end{aligned} \quad (27)$$

We choose a piece-wise linear approximation in x and a piece-wise constant approximation in ε and θ

$$\tilde{f}_s(t, x, \varepsilon, \theta) = a_{i,k,n}^s(t) + \frac{2(x - x_i)}{\Delta x} b_{i,k,n}^s(t), \quad \forall (x, \varepsilon, \theta) \in C_{i,k,n}. \quad (28)$$

An orthogonal basis for the polynomial space $P^{1,0,0}(C_{i,k,n})$ is

$$\tilde{v}^0(x, \varepsilon, \theta) = 1, \quad \tilde{v}^1(x, \varepsilon, \theta) = \frac{2(x - x_i)}{\Delta x}. \quad (29)$$

The reconstruction of the approximation of f_s in all the computational domain is

$$\tilde{f}_s = \sum_{i=1}^{N_x} \sum_{k=1}^{N_\varepsilon} \sum_{n=1}^{N_\theta} \left[a_{i,k,n}^s(t) + \frac{2(x - x_i)}{\Delta x} b_{i,k,n}^s(t) \right] \chi_{C_{i,k,n}}(x, \varepsilon, \theta), \quad (30)$$

where $\chi_{C_{i,k,n}}(\cdot, \cdot, \cdot)$ represents the characteristic function of $C_{i,k,n}$.

Now we project the equations in the finite dimensional space \tilde{V} by substituting the basis elements \tilde{v}^0 and \tilde{v}^1 to \tilde{v} in the approximate weak formulation (27). For all $i = 1, 2, \dots, N_x$, for all $k = 1, 2, \dots, N_\varepsilon$ and for all $n = 1, 2, \dots, N_\theta$ we discretize each term of equation separately.

4.1 Discretization of the free-streaming case

The terms involving the time derivatives become

$$\int_{C_{i,k,n}} \frac{\varepsilon}{(\hbar v_F)^2} \frac{\partial \tilde{f}_s}{\partial t} dx d\varepsilon d\theta = \Delta x \Delta \theta \frac{\varepsilon_{k+1/2}^2 - \varepsilon_{k-1/2}^2}{2(\hbar v_F)^2} \frac{d}{dt} a_{i,k,n}^s(t) \quad (31)$$

if we choose \tilde{v}^0 as test function while become

$$\begin{aligned} & \int_{C_{i,k,n}} \frac{2(x - x_i)}{\Delta x} \frac{\varepsilon}{(\hbar v_F)^2} \frac{\partial \tilde{f}_s}{\partial t} dx d\varepsilon d\theta \\ &= \Delta \theta \frac{\varepsilon_{k+1/2}^2 - \varepsilon_{k-1/2}^2}{2(\hbar v_F)^2} \left[\frac{d}{dt} a_{i,k,n}^s(t) \int_{x_{i-1/2}}^{x_{i+1/2}} \frac{2(x - x_i)}{\Delta x} dx + \frac{d}{dt} b_{i,k,n}^s(t) \int_{x_{i-1/2}}^{x_{i+1/2}} \frac{4(x - x_i)^2}{(\Delta x)^2} dx \right] \\ &= \frac{\Delta x}{3} \Delta \theta \frac{\varepsilon_{k+1/2}^2 - \varepsilon_{k-1/2}^2}{2(\hbar v_F)^2} \frac{d}{dt} b_{i,k,n}^s(t). \end{aligned} \quad (32)$$

if we choose \tilde{v}^1 as test function.

The terms involving the space derivatives, for $m = 0, 1$ can be written as

$$\begin{aligned} & \int_{C_{i,k,n}} \tilde{v}^m \left\{ s \frac{v_F}{(\hbar v_F)^2} \varepsilon \cos \theta \frac{\partial \tilde{f}_s}{\partial x} \right\} dx d\varepsilon d\theta \\ &= s \frac{v_F}{(\hbar v_F)^2} \int_{\varepsilon_{k-1/2}}^{\varepsilon_{k+1/2}} \int_{\theta_{n-1/2}}^{\theta_{n+1/2}} \int_{x_{i-1/2}}^{x_{i+1/2}} \left[\frac{\partial}{\partial x} \left(\tilde{v}^m \varepsilon \cos \theta \tilde{f}_s \right) - \frac{\partial \tilde{v}^m}{\partial x} \varepsilon \cos \theta \tilde{f}_s \right] dx d\theta d\varepsilon. \end{aligned} \quad (33)$$

In particular, for \tilde{v}^0 , we have

$$\begin{aligned} & \int_{C_{i,k,n}} s \frac{v_F}{(\hbar v_F)^2} \varepsilon \cos \theta \frac{\partial \tilde{f}_s}{\partial x} dx d\varepsilon d\theta \\ &= s \frac{v_F}{(\hbar v_F)^2} \int_{\varepsilon_{k-1/2}}^{\varepsilon_{k+1/2}} \int_{\theta_{n-1/2}}^{\theta_{n+1/2}} \varepsilon \cos \theta \left[\tilde{f}_s(t, x_{i+1/2}, \varepsilon, \theta) - f_s(t, x_{i-1/2}, \varepsilon, \theta) \right] d\theta d\varepsilon, \end{aligned} \quad (34)$$

and, for \tilde{v}^1 , we have

$$\begin{aligned} & \int_{C_{i,k,n}} s \frac{v_F}{(\hbar v_F)^2} \frac{2(x - x_i)}{\Delta x} \varepsilon \cos \theta \frac{\partial f_s}{\partial x} dx d\varepsilon d\theta \\ &= s \frac{v_F}{(\hbar v_F)^2} \int_{\varepsilon_{k-1/2}}^{\varepsilon_{k+1/2}} \int_{\theta_{n-1/2}}^{\theta_{n+1/2}} \varepsilon \cos \theta \left[\tilde{f}_s(t, x_{i+1/2}, \varepsilon, \theta) + \tilde{f}_s(t, x_{i-1/2}, \varepsilon, \theta) - 2a_{i,k,n}^s(t) \right] d\theta d\varepsilon. \end{aligned} \quad (35)$$

Since \tilde{f}_s is discontinuous on the boundaries of the cells we must replace the flux $\tilde{f}_s(t, x_{i+1/2}, \varepsilon, \theta)$ by a numerical flux depending on the two values of \tilde{f}_s along $\{x_{i+1/2}\} \times [\varepsilon_{k-1/2}, \varepsilon_{k+1/2}] \times [\theta_{n-1/2}, \theta_{n+1/2}]$, that is, for all $(\varepsilon, \theta) \in [\varepsilon_{k-1/2}, \varepsilon_{k+1/2}] \times [\theta_{n-1/2}, \theta_{n+1/2}]$

$$\tilde{f}_s(t, x_{i+1/2}, \varepsilon, \theta) = F_{i+1/2,k,n}^s \left(\tilde{f}_s(t, x_{i+1/2}^-, \varepsilon, \theta), \tilde{f}_s(t, x_{i+1/2}^+, \varepsilon, \theta) \right),$$

where (see Fig. 4)

$$\begin{aligned} \tilde{f}_s(t, x_{i+1/2}^-, \varepsilon, \theta) &\approx a_{i,k,n}^s(t) + b_{i,k,n}^s(t) =: \tilde{f}_{i+1/2,k,n}^{s,-}(t), \\ \tilde{f}_s(t, x_{i+1/2}^+, \varepsilon, \theta) &\approx a_{i+1,k,n}^s(t) - b_{i+1,k,n}^s(t) =: \tilde{f}_{i+1/2,k,n}^{s,+}(t), \end{aligned} \quad (36)$$

and $F_{i+1/2,k,n}^s$ a suitable numerical recipe.

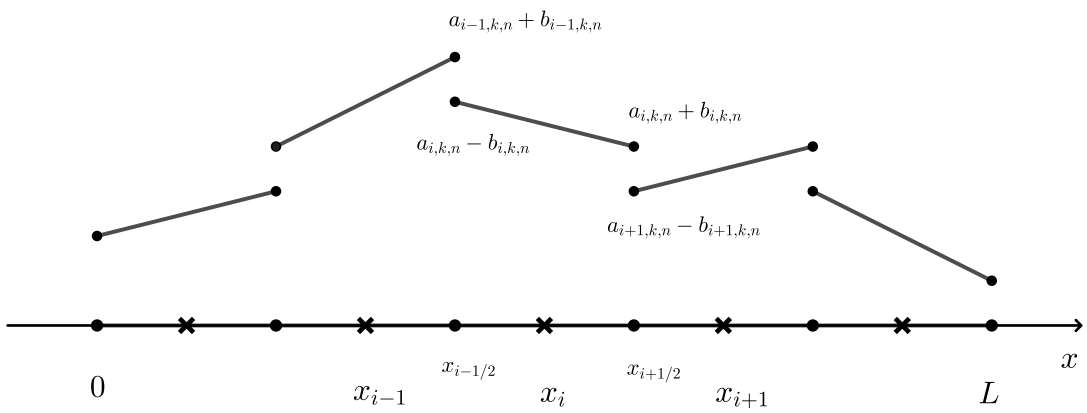


Figure 4: Discretization with respect to x where ε and θ are fixed.

Therefore, eq. (34) becomes

$$\int_{C_{i,k,n}} s \frac{v_F}{(\hbar v_F)^2} \varepsilon \cos \theta \frac{\partial \tilde{f}_s}{\partial x} dx d\varepsilon d\theta = \left[F_{i+1/2,k,n}^s(t) - F_{i-1/2,k,n}^s(t) \right] M_{k,n}^s, \quad (37)$$

while eq. (35) reads

$$\int_{C_{i,k,n}} s \frac{v_F}{(\hbar v_F)^2} \varepsilon \cos \theta \frac{\partial \tilde{f}_s}{\partial x} dx d\varepsilon d\theta = \left[F_{i+1/2,k,n}^s(t) + F_{i-1/2,k,n}^s(t) - 2a_{i,k,n}^s(t) \right] M_{k,n}^s, \quad (38)$$

where we have set

$$M_{k,n}^s := s \frac{v_F}{(\hbar v_F)^2} \int_{\varepsilon_{k-1/2}}^{\varepsilon_{k+1/2}} \int_{\theta_{n-1/2}}^{\theta_{n+1/2}} \varepsilon \cos \theta d\theta d\varepsilon = s \frac{v_F}{(\hbar v_F)^2} \frac{\varepsilon_{k+1/2}^2 - \varepsilon_{k-1/2}^2}{2} \frac{\sin \theta_{n+1/2} - \sin \theta_{n-1/2}}{2}. \quad (39)$$

We remark that the reconstructions at $x_{1/2} = 0$ and $x_{N_x+1/2} = L$ are given by the boundary conditions. Since the equation is linear with respect to x , as numerical flux function $F_{i+1/2,k,n}^s$ we adopt

$$F_{i+1/2,k,n}^s \left(\tilde{f}_{i+1/2,k,n}^{s,-}, \tilde{f}_{i+1/2,k,n}^{s,+} \right) = \frac{\tilde{f}_{i+1/2,k,n}^{s,-} + \tilde{f}_{i+1/2,k,n}^{s,+}}{2} - \frac{1-\eta}{2} \text{sign}(M_{k,n}^s) \left(\tilde{f}_{i+1/2,k,n}^{s,-} - \tilde{f}_{i+1/2,k,n}^{s,+} \right), \quad (40)$$

where $0 \leq \eta \leq 1$ for stability [14]. Observe that $\eta = 1$ returns the central flux and $\eta = 0$ the upwind one. The most appropriate value depends on the specific equation and in many cases it must be determined numerically.

4.2 Discretization of the drift term

In order to approximate the drift term, we first consider a piece-wise linear interpolation of the electrostatic potential ϕ , that is

$$\phi(x, y_{gr}) \approx \phi_{i-1/2,j_{gr}} + \frac{x - x_{i-1/2}}{\Delta x} (\phi_{i+1/2,j_{gr}} - \phi_{i-1/2,j_{gr}}), \quad \forall x \in [x_{i-1/2}, x_{i+1/2}], \quad (41)$$

where j_{gr} is the index of the discretization corresponding to y_{gr} . Consequently, the approximation of the electrical field E_x reads

$$E_x(x, y_{gr}) = -\frac{\partial \phi(x, y_{gr})}{\partial x} \approx -\frac{\phi_{i+1/2,j_{gr}} - \phi_{i-1/2,j_{gr}}}{\Delta x}, \quad \forall x \in [x_{i-1/2}, x_{i+1/2}]. \quad (42)$$

Therefore, we set

$$E_x^i = -\frac{\phi_{i+1/2,j_{gr}} - \phi_{i-1/2,j_{gr}}}{\Delta x}, \quad \forall x \in [x_{i-1/2}, x_{i+1/2}]. \quad (43)$$

Overall, the approximation of the drift term reads

$$\begin{aligned} & \int_{C_{i,k,n}} \tilde{v}^m \left\{ -eE_x \frac{v_F}{(\hbar v_F)^2} \left[\frac{\partial}{\partial \varepsilon} (\varepsilon \cos \theta \tilde{f}_s) - \frac{\partial}{\partial \theta} (\sin \theta \tilde{f}_s) \right] \right\} dx d\varepsilon d\theta \\ & \approx -\frac{eE_x^i v_F}{(\hbar v_F)^2} \int_{x_{i-1/2}}^{x_{i+1/2}} \tilde{v}^m \left\{ \int_{\theta_{n-1/2}}^{\theta_{n+1/2}} \left[\varepsilon \cos \theta \tilde{f}_s \right]_{\varepsilon_{k-1/2}}^{\varepsilon_{k+1/2}} d\theta - \int_{\varepsilon_{k-1/2}}^{\varepsilon_{k+1/2}} \left[\sin \theta \tilde{f}_s \right]_{\theta_{n-1/2}}^{\theta_{n+1/2}} d\varepsilon \right\} dx. \end{aligned} \quad (44)$$

On account of the fact that \tilde{f}_s is not defined for $\varepsilon = \varepsilon_{k\pm 1/2}$ and $\theta = \theta_{n\pm 1/2}$, we replace it with a numerical flux function. Since we adopt a piece-wise constant approximation with respect to ε and θ , the adoption of a numerical flux function reflects on the degrees of freedom of the DG approximation directly. In particular, we have

$$\begin{aligned} \tilde{f}_s(t, x, \varepsilon_{k\pm 1/2}, \theta) &= a_{i,k\pm 1/2,n}^s + \frac{2(x - x_i)}{\Delta x} b_{i,k\pm 1/2,n}^s \quad \forall x \in [x_{i-1/2}, x_{i+1/2}], \quad \forall \theta \in [\theta_{n-1/2}, \theta_{n+1/2}], \\ \tilde{f}_s(t, x, \varepsilon, \theta_{n\pm 1/2}) &= a_{i,k,n\pm 1/2}^s + \frac{2(x - x_i)}{\Delta x} b_{i,k,n\pm 1/2}^s \quad \forall x \in [x_{i-1/2}, x_{i+1/2}], \quad \forall \varepsilon \in [\varepsilon_{k-1/2}, \varepsilon_{k+1/2}]. \end{aligned} \quad (45)$$

Therefore, for $m = 0$, the right hand side of equation (44) becomes

$$\begin{aligned} & -\frac{eE_x^i v_F}{(\hbar v_F)^2} \Delta x \left\{ \left[\varepsilon_{k+1/2} a_{i,k+1/2,n}^s - \varepsilon_{k-1/2} a_{i,k-1/2,n}^s \right] (\sin \theta_{n+1/2} - \sin \theta_{n-1/2}) \right. \\ & \left. - \left[\sin \theta_{n+1/2} a_{i,k,n+1/2}^s - \sin \theta_{n-1/2} a_{i,k,n-1/2}^s \right] \Delta \varepsilon \right\}, \end{aligned} \quad (46)$$

and, for $m = 1$, it reads

$$-\frac{eE_x^i v_F}{(\hbar v_F)^2} \frac{\Delta x}{3} \left\{ \left[\varepsilon_{k+1/2} b_{i,k+1/2,n}^s - \varepsilon_{k-1/2} b_{i,k-1/2,n}^s \right] (\sin \theta_{n+1/2} - \sin \theta_{n-1/2}) \right. \\ \left. - \left[\sin \theta_{n+1/2} b_{i,k,n+1/2}^s - \sin \theta_{n-1/2} b_{i,k,n-1/2}^s \right] \Delta \varepsilon \right\}. \quad (47)$$

The quantities $a_{i,k\pm 1/2,n}^s$, $a_{i,k,n\pm 1/2}^s$, $b_{i,k\pm 1/2,n}^s$, and $b_{i,k,n\pm 1/2}^s$ represent the numerical flux functions and depend on the nearest neighbor degrees of freedom. For a linear equation, the simplest choice is to adopt the numerical flux (40). Following [25], we assume, instead, a uniformly non-oscillatory (UNO) piece-wise linear reconstruction. For a generic 1D situation, such an approximation of a function $g(z)$ in $z_{j+1/2}$ is obtained by a numerical flux function $g_{j+1/2} = g_{j+1/2}(g_{j-1}, g_j, g_{j+1}, g_{j+2})$, where g_j indicates the cell average of g in $g_j - \frac{\Delta z}{2}, g_j + \frac{\Delta z}{2}$. Once identified the wind velocity w , by approximating with the first term of the Taylor expansion, we have

$$g_{j+1/2} \approx \begin{cases} g_j + \frac{\Delta z}{2} g'_j & \text{if } w > 0 \\ g_{j+1} - \frac{\Delta z}{2} g'_{j+1} & \text{if } w < 0 \end{cases} \quad (48)$$

where

$$g'_j = \text{MinMod} \left(\frac{g_j - g_{j-1}}{\Delta z}, \frac{g_{j+1} - g_j}{\Delta z} \right), \quad (49)$$

with

$$\text{MinMod}(\alpha, \beta) = \begin{cases} \min(|\alpha|, |\beta|) \text{sgn}(\alpha) & \text{if } \alpha \beta > 0 \\ 0 & \text{otherwise} \end{cases} \quad (50)$$

In the case of equations (46) and (47), we assume as wind velocity related to $a_{i,k+1/2,n}^s$ and $b_{i,k+1/2,n}^s$ the quantity

$$w_{i,k+1/2,n} = \text{sgn}(-E_x^i (\mathbf{i} \cdot \hat{\mathbf{n}}_{k+1/2,n}) (\sin \theta_{n+1/2} - \sin \theta_{n-1/2})), \quad (51)$$

and, as wind velocity related to $a_{i,k,n+1/2}^s$ and $b_{i,k,n+1/2}^s$ the quantity

$$w_{i,k,n+1/2} = \text{sgn}(\Delta \varepsilon E_x^i (\mathbf{i} \cdot \hat{\mathbf{n}}_{k,n+1/2})), \quad (52)$$

where $\hat{\mathbf{n}}_{k+1/2,n}$ is the outer normal direction of the edge of the cell $C_{i,k,n}$ identified by $\varepsilon = \varepsilon_{k+1/2}$, and $\hat{\mathbf{n}}_{k,n+1/2}$ is the outer normal direction of the edge of the cell $C_{i,k,n}$ identified by $\theta = \theta_{n+1/2}$, see Fig. 5. Since the above discretization holds for each $k = 0, 1, \dots, N_\varepsilon$ and for each $n = 0, 1, \dots, N_\theta$, we need to extend the grid with two ghost cells to the ends of both the radial and the angular direction. Therefore, in addition, we assume zero radial inflow at $\varepsilon = 0$ and zero radial outflow at $\varepsilon = \varepsilon_{max}$, while we assume periodic boundary conditions with respect to the angle. The choice described above assures an higher accuracy with respect to the flux (40) and the total variation diminishing (TVD) property [31]. Although it is desirable for accuracy to adopt a piece-wise DG discretization also with respect to the energy and the angle, our choice aims to maintain a moderate computational costs.

4.3 Discretization of the collision term

In order to approximate the collision term, to avoid cumbersome notation, we remark that it can be expressed as

$$Q(f_s, f_{-s}) = \sum_{s'} \sum_{\lambda} \int_0^{+\infty} d\varepsilon' \int_0^{2\pi} d\theta' \frac{\varepsilon'}{(\hbar v_F)^2} \left[S_{s',s}^{(\lambda)}(\varepsilon', \theta', \varepsilon, \theta) f_{s'}(t, x, \varepsilon', \theta') (1 - f_s(t, x, \varepsilon, \theta)) \right. \\ \left. - S_{s,s'}^{(\lambda)}(\varepsilon, \theta, \varepsilon', \theta') f_s(t, x, \varepsilon, \theta) (1 - f_{s'}(t, x, \varepsilon', \theta')) \right]. \quad (53)$$

where the index λ runs over the possible types of scattering.

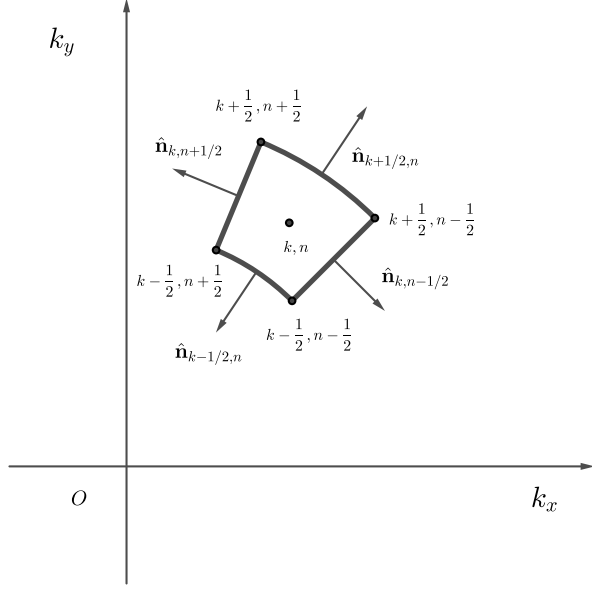


Figure 5: Representation of a generic cell for the computation of the numerical fluxes.

We set

$$\begin{aligned}
A_{s',s}^{k',n'} &= \frac{1}{(\hbar v_F)^4} \int_{\varepsilon_{k-\frac{1}{2}}}^{\varepsilon_{k+\frac{1}{2}}} d\varepsilon \int_{\theta_{n-\frac{1}{2}}}^{\theta_{n+\frac{1}{2}}} d\theta \int_{\varepsilon_{k'-\frac{1}{2}}}^{\varepsilon_{k'+\frac{1}{2}}} d\varepsilon' \int_{\theta_{n'-\frac{1}{2}}}^{\theta_{n'+\frac{1}{2}}} d\theta' \varepsilon' \varepsilon \sum_{\lambda} \left[D^{(\lambda)} + E^{(\lambda)} \cos(\theta - \theta') \right] \\
&\times \left[(n_{\mathbf{q}}^{(\lambda)} + 1) \delta(s' \varepsilon' - s \varepsilon + \hbar \omega^{(\lambda)}) + n_{\mathbf{q}}^{(\lambda)} \delta(s' \varepsilon' - s \varepsilon - \hbar \omega^{(\lambda)}) \right] \\
&= \frac{1}{(\hbar v_F)^4} \sum_{\lambda} \int_{\theta_{n-\frac{1}{2}}}^{\theta_{n+\frac{1}{2}}} d\theta \int_{\theta_{n'-\frac{1}{2}}}^{\theta_{n'+\frac{1}{2}}} d\theta' \left[D^{(\lambda)} + E^{(\lambda)} \cos(\theta - \theta') \right] \\
&\times \int_{\varepsilon_{k-\frac{1}{2}}}^{\varepsilon_{k+\frac{1}{2}}} d\varepsilon \int_{\varepsilon_{k'-\frac{1}{2}}}^{\varepsilon_{k'+\frac{1}{2}}} d\varepsilon' \varepsilon' \varepsilon \left[(n_{\mathbf{q}}^{(\lambda)} + 1) \delta \left(\varepsilon' - \frac{s}{s'} \varepsilon + \frac{\hbar \omega^{(\lambda)}}{s'} \right) + n_{\mathbf{q}}^{(\lambda)} \delta \left(\varepsilon' - \frac{s}{s'} \varepsilon - \frac{\hbar \omega^{(\lambda)}}{s'} \right) \right]
\end{aligned}$$

where the coefficients $D^{(\lambda)}$ and $E^{(\lambda)}$ are related to the scattering rates.

We have

$$\begin{aligned}
&\int_{\theta_{n-\frac{1}{2}}}^{\theta_{n+\frac{1}{2}}} d\theta \int_{\theta_{n'-\frac{1}{2}}}^{\theta_{n'+\frac{1}{2}}} d\theta' \left[D^{(\lambda)} + E^{(\lambda)} \cos(\theta - \theta') \right] \\
&= D^{(\lambda)} \Delta \theta^2 + 4E^{(\lambda)} \sin^2 \left(\frac{\Delta \theta}{2} \right) \cos \left(\frac{\theta_{n-\frac{1}{2}} + \theta_{n+\frac{1}{2}}}{2} - \frac{\theta_{n'-\frac{1}{2}} + \theta_{n'+\frac{1}{2}}}{2} \right)
\end{aligned}$$

and

$$\begin{aligned}
&\int_{\varepsilon_{k-\frac{1}{2}}}^{\varepsilon_{k+\frac{1}{2}}} d\varepsilon \int_{\mathbb{R}} d\varepsilon' \chi_{\left[\varepsilon_{k'-\frac{1}{2}}, \varepsilon_{k'+\frac{1}{2}} \right]}(\varepsilon') \varepsilon' \varepsilon \left[(n_{\mathbf{q}}^{(\lambda)} + 1) \delta \left(\varepsilon' - \frac{s}{s'} \varepsilon + \frac{\hbar \omega^{(\lambda)}}{s'} \right) + n_{\mathbf{q}}^{(\lambda)} \delta \left(\varepsilon' - \frac{s}{s'} \varepsilon - \frac{\hbar \omega^{(\lambda)}}{s'} \right) \right] \\
&= \int_{\varepsilon_{k-\frac{1}{2}}}^{\varepsilon_{k+\frac{1}{2}}} d\varepsilon \left\{ (n_{\mathbf{q}}^{(\lambda)} + 1) \varepsilon \left(\frac{s}{s'} \varepsilon - \frac{\hbar \omega^{(\lambda)}}{s'} \right) \chi_{\left[\varepsilon_{k'-\frac{1}{2}}, \varepsilon_{k'+\frac{1}{2}} \right]} \left(\frac{s}{s'} \varepsilon - \frac{\hbar \omega^{(\lambda)}}{s'} \right) \right. \\
&\quad \left. n_{\mathbf{q}}^{(\lambda)} \varepsilon \left(\frac{s}{s'} \varepsilon + \frac{\hbar \omega^{(\lambda)}}{s'} \right) \chi_{\left[\varepsilon_{k'-\frac{1}{2}}, \varepsilon_{k'+\frac{1}{2}} \right]} \left(\frac{s}{s'} \varepsilon + \frac{\hbar \omega^{(\lambda)}}{s'} \right) \right\} \\
&= (n_{\mathbf{q}}^{(\lambda)} + 1) \left[\frac{s}{s'} \frac{\varepsilon^3}{3} - \frac{\hbar \omega^{(\lambda)} \varepsilon^2}{s'} \frac{1}{2} \right]_{\min I^-}^{\max I^-} + n_{\mathbf{q}}^{(\lambda)} \left[\frac{s}{s'} \frac{\varepsilon^3}{3} + \frac{\hbar \omega^{(\lambda)} \varepsilon^2}{s'} \frac{1}{2} \right]_{\min I^+}^{\max I^+},
\end{aligned}$$

where

$$I^\pm = \left\{ \varepsilon \in \mathbb{R}_0^+ : \varepsilon_{k-\frac{1}{2}} \leq \varepsilon \leq \varepsilon_{k+\frac{1}{2}}, \varepsilon_{k'-\frac{1}{2}} \leq \varepsilon \leq \varepsilon_{k'+\frac{1}{2}} \right\}.$$

Therefore, the approximation of the collision term reads

$$\begin{aligned} \int_{C_{i,k,n}} \tilde{v}^m \frac{\varepsilon}{(\hbar v_F)^2} Q(\tilde{f}_s, \tilde{f}_{-s}) dx d\varepsilon d\theta &= \sum_{s'}^{N_\varepsilon} \sum_{k'=1}^{N_\theta} \sum_{n'=1}^{N_\theta} \int_{x_{i-1/2}}^{x_{i+1/2}} dx \tilde{v}^m \left[A_{s',s}^{k',n'} \tilde{f}_{s'}(t, x, \varepsilon', \theta') (1 - \tilde{f}_s(t, x, \varepsilon, \theta)) \right. \\ &\quad \left. - A_{s,s'}^{k',n'} \tilde{f}_s(t, x, \varepsilon, \theta) (1 - \tilde{f}_{s'}(t, x, \varepsilon', \theta')) \right] \\ &= \sum_{s'}^{N_\varepsilon} \sum_{k'=1}^{N_\theta} \sum_{n'=1}^{N_\theta} \int_{x_{i-1/2}}^{x_{i+1/2}} dx \tilde{v}^m \left\{ A_{s',s}^{k',n'} \left[a_{i,k',n'}^{s'}(t) + \frac{2(x-x_i)}{\Delta x} b_{i,k',n'}^{s'}(t) \right] \left[1 - a_{i,k,n}^s(t) - \frac{2(x-x_i)}{\Delta x} b_{i,k,n}^s(t) \right] \right. \\ &\quad \left. - A_{s,s'}^{k',n'} \left[a_{i,k,n}^s(t) + \frac{2(x-x_i)}{\Delta x} b_{i,k,n}^s(t) \right] \left[1 - a_{i,k',n'}^{s'}(t) - \frac{2(x-x_i)}{\Delta x} b_{i,k',n'}^{s'}(t) \right] \right\} \\ &= \sum_{s'}^{N_\varepsilon} \sum_{k'=1}^{N_\theta} \sum_{n'=1}^{N_\theta} \int_{x_{i-1/2}}^{x_{i+1/2}} dx \tilde{v}^m \left\{ \left[A_{s',s}^{k',n'} a_{i,k',n'}^{s'}(t) (1 - a_{i,k,n}^s(t)) - A_{s,s'}^{k',n'} a_{i,k,n}^s(t) (1 - a_{i,k',n'}^{s'}(t)) \right] \right. \\ &\quad \left. - \frac{2(x-x_i)}{\Delta x} \left[A_{s',s}^{k',n'} \left(a_{i,k',n'}^{s'}(t) b_{i,k,n}^s(t) - (1 - a_{i,k,n}^s(t)) b_{i,k',n'}^{s'}(t) \right) \right. \right. \\ &\quad \left. \left. - A_{s,s'}^{k',n'} \left(a_{i,k,n}^s(t) b_{i,k',n'}^{s'}(t) - (1 - a_{i,k',n'}^{s'}(t)) b_{i,k,n}^s(t) \right) \right] \right. \\ &\quad \left. - \frac{4(x-x_i)^2}{\Delta x^2} \left[A_{s',s}^{k',n'} b_{i,k',n'}^{s'}(t) b_{i,k,n}^s(t) - A_{s,s'}^{k',n'} b_{i,k,n}^s(t) b_{i,k',n'}^{s'}(t) \right] \right\}. \end{aligned}$$

Specifically, for $m = 0$ we get

$$\begin{aligned} \int_{C_{i,k,n}} \frac{\varepsilon}{(\hbar v_F)^2} Q(\tilde{f}_s, \tilde{f}_{-s}) dx d\varepsilon d\theta &= \sum_{s'}^{N_\varepsilon} \sum_{k'=1}^{N_\theta} \sum_{n'=1}^{N_\theta} \Delta x \left\{ \left[A_{s',s}^{k',n'} a_{i,k',n'}^{s'}(t) (1 - a_{i,k,n}^s(t)) - A_{s,s'}^{k',n'} a_{i,k,n}^s(t) (1 - a_{i,k',n'}^{s'}(t)) \right] \right. \\ &\quad \left. - \frac{1}{3} \left[A_{s',s}^{k',n'} b_{i,k',n'}^{s'}(t) b_{i,k,n}^s(t) - A_{s,s'}^{k',n'} b_{i,k,n}^s(t) b_{i,k',n'}^{s'}(t) \right] \right\}, \end{aligned}$$

and for $m = 1$ we obtain

$$\begin{aligned} \int_{C_{i,k,n}} \frac{2(x-x_i)}{\Delta x} \frac{\varepsilon}{(\hbar v_F)^2} Q(\tilde{f}_s, \tilde{f}_{-s}) dx d\varepsilon d\theta &= -\frac{\Delta x}{3} \sum_{s'}^{N_\varepsilon} \sum_{k'=1}^{N_\theta} \sum_{n'=1}^{N_\theta} \left[A_{s',s}^{k',n'} \left(a_{i,k',n'}^{s'}(t) b_{i,k,n}^s(t) - (1 - a_{i,k,n}^s(t)) b_{i,k',n'}^{s'}(t) \right) \right. \\ &\quad \left. - A_{s,s'}^{k',n'} \left(a_{i,k,n}^s(t) b_{i,k',n'}^{s'}(t) - (1 - a_{i,k',n'}^{s'}(t)) b_{i,k,n}^s(t) \right) \right] \end{aligned}$$

We remark that a piece-wise linear DG discretization with respect to the energy and the angle leads to the computation of 16 families of coefficients with a structure similar to $A_{s',s}^{k,n}$ for each s and s' [32].

Considering all the terms discussed above, we obtain a set of $4N_x N_\varepsilon N_\theta$ ordinary differential equations. For the time discretization we adopt a third order TVD Runge-Kutta method [33].

We remark that the electron distribution functions must be between 0 and 1 [34]. This cannot be automatically guaranteed by adopting the DG discretization described above. To overcome this issue we

adopt the maximum-principle-satisfying scheme introduced in [35]. It consists of a linear scaling around the cell average of the reconstruction. If

$$\tilde{f}_s(t, x, \varepsilon, \theta) = a_{i,k,n}^s(t) + \frac{2(x - x_i)}{\Delta x} b_{i,k,n}^s(t), \quad \forall (x, \varepsilon, \theta) \in C_{i,k,n} \quad (54)$$

is the reconstruction of f_s in $C_{i,k,n}$ than we define

$$\tilde{\tilde{f}}_s(t, x, \varepsilon, \theta) = a_{i,k,n}^s(t) + \vartheta \frac{2(x - x_i)}{\Delta x} b_{i,k,n}^s(t), \quad \forall (x, \varepsilon, \theta) \in C_{i,k,n} \quad (55)$$

where ϑ is

$$\vartheta = \min \left\{ \frac{|1 - a_{i,k,n}^s(t)|}{|M - a_{i,k,n}^s(t)|}, \frac{|a_{i,k,n}^s(t)|}{|m - a_{i,k,n}^s(t)|}, 1 \right\} \quad (56)$$

and M, m are the maximum and the minimum of $\tilde{f}_s(t, x, \varepsilon, \theta)$ in $C_{i,k,n}$. Since the reconstruction is linear they are

$$\begin{aligned} M &= \max \{a_{i,k,n}^s(t) - b_{i,k,n}^s(t), a_{i,k,n}^s(t) + b_{i,k,n}^s(t)\}, \\ m &= \min \{a_{i,k,n}^s(t) - b_{i,k,n}^s(t), a_{i,k,n}^s(t) + b_{i,k,n}^s(t)\}. \end{aligned} \quad (57)$$

To compute the macroscopic physical quantities we evaluate the cell averages with respect to x , which is equivalent to the piecewise constant reconstruction. For electrons we obtain

$$\begin{aligned} n_i(t) = n(t, x_i) &\approx \frac{g_s g_v}{(2\pi)^2} \sum_{k=1}^{N_\varepsilon} \sum_{n=1}^{N_\theta} a_{i,k,n}^+ \bar{N}_{k,n}, & \text{(electron density)} \\ j_i^{n,x}(t) = j^{n,x}(t, x_i) &\approx -e \frac{g_s g_v}{(2\pi)^2} \sum_{k=1}^{N_\varepsilon} \sum_{n=1}^{N_\theta} a_{i,k,n}^+ \bar{R}_{k,n}, & \text{(electron current density)} \\ \mathcal{E}_i^n(t) = \mathcal{E}^n(t, x_i) &\approx \frac{g_s g_v}{(2\pi)^2} \sum_{k=1}^{N_\varepsilon} \sum_{n=1}^{N_\theta} a_{i,k,n}^+ \bar{T}_{k,n}. & \text{(electron energy density)} \end{aligned} \quad (58)$$

The coefficients $\bar{N}_{k,n}$, $\bar{R}_{k,n}$ and $\bar{T}_{k,n}$ are the integrals of the weight functions evaluated on the generic cell of the momentum space:

$$\begin{aligned} \bar{N}_{k,n} &= \frac{\Delta\theta}{2(\hbar v_F)^2} \left(\varepsilon_{k+\frac{1}{2}}^2 - \varepsilon_{k-\frac{1}{2}}^2 \right), \\ \bar{R}_{k,n} &= \frac{v_F}{2(\hbar v_F)^2} \left(\varepsilon_{k+\frac{1}{2}}^2 - \varepsilon_{k-\frac{1}{2}}^2 \right) \left(\sin \theta_{n+\frac{1}{2}} - \sin \theta_{n-\frac{1}{2}} \right), \\ \bar{T}_{k,n} &= \frac{1}{3(\hbar v_F)^2} \left(\varepsilon_{k+\frac{1}{2}}^3 - \varepsilon_{k-\frac{1}{2}}^3 \right). \end{aligned} \quad (59)$$

Similarly, for holes we have

$$\begin{aligned} p_i(t) = p(t, x_i) &\approx \frac{g_s g_v}{(2\pi)^2} \sum_{k=1}^{N_\varepsilon} \sum_{n=1}^{N_\theta} (1 - a_{i,k,n}^-) \bar{N}_{k,n}, & \text{(hole density)} \\ j_i^{p,x}(t) = j^{p,x}(t, x_i) &\approx e \frac{g_s g_v}{(2\pi)^2} \sum_{k=1}^{N_\varepsilon} \sum_{n=1}^{N_\theta} (1 - a_{i,k,n}^-) \bar{R}_{k,n}, & \text{(hole current density)} \\ \mathcal{E}_i^p(t) = \mathcal{E}^p(t, x_i) &\approx \frac{g_s g_v}{(2\pi)^2} \sum_{k=1}^{N_\varepsilon} \sum_{n=1}^{N_\theta} (1 - a_{i,k,n}^-) \bar{T}_{k,n}. & \text{(hole energy density)} \end{aligned} \quad (60)$$

For plotting reason, the average quantities are also computed at $x = 0$ and $x = L$ by using the boundary conditions.

To compute the right hand side of the Poisson equation at the edges of the mesh, i.e. $h_{i+\frac{1}{2},j+\frac{1}{2}}$, we first calculate the electron and hole density both at the left and right reconstruction of the distribution,

$$\begin{aligned} n_{i+\frac{1}{2}}^- &= \frac{g_s g_v}{(2\pi)^2} \sum_{k=1}^{N_\varepsilon} \sum_{n=1}^{N_\theta} (a_{i,k,n}^+ + b_{i,k,n}^+) \bar{N}_{k,n}, \\ n_{i+\frac{1}{2}}^+ &= \frac{g_s g_v}{(2\pi)^2} \sum_{k=1}^{N_\varepsilon} \sum_{n=1}^{N_\theta} (a_{i+1,k,n}^+ - b_{i+1,k,n}^+) \bar{N}_{k,n}, \\ p_{i+\frac{1}{2}}^- &= \frac{g_s g_v}{(2\pi)^2} \sum_{k=1}^{N_\varepsilon} \sum_{n=1}^{N_\theta} [1 - (a_{i,k,n}^- + b_{i,k,n}^-)] \bar{N}_{k,n}, \\ p_{i+\frac{1}{2}}^+ &= \frac{g_s g_v}{(2\pi)^2} \sum_{k=1}^{N_\varepsilon} \sum_{n=1}^{N_\theta} [1 - (a_{i+1,k,n}^- - b_{i+1,k,n}^-)] \bar{N}_{k,n}, \end{aligned} \quad (61)$$

and then average the quantities at the two sides of each edge

$$\begin{aligned} n_{i+\frac{1}{2}} &= \frac{1}{2} \left(n_{i+\frac{1}{2}}^- + n_{i+\frac{1}{2}}^+ \right), \\ p_{i+\frac{1}{2}} &= \frac{1}{2} \left(p_{i+\frac{1}{2}}^- + p_{i+\frac{1}{2}}^+ \right). \end{aligned} \quad (62)$$

5 Simulation results

In this section we use the numerical approach presented above to simulate the cases described in Sec. 3, first investigating the accuracy of the numerical method adopted.

5.1 Test case 1: suspended monolayer graphene

The study of the convergence of the numerical scheme has been addressed comparing the simulation results of the macroscopic quantities at stationary regime on different meshes with respect to the variables x , ε and θ . The analysis is performed in the physical situation of the test case of Fig. 1. The device length is 100 nm and the Fermi level in the boundary conditions is set to 0.25 eV. Since the graphene layer is suspended, we do not consider the electron-substrate collision term $Q^{(el-sub)}$. We adopt the same physical parameters used in Section 5 with an electric field of 1 V/ μ m. The time at which we compare the results is 1 ps, when the stationary regime is already reached.

First we discuss the convergence of the scheme with respect to x analyzing electron density, mean velocity, and mean energy. We consider a fixed discretization of $N_\varepsilon = 80$ and $N_\theta = 32$ in the energy-angle space. Let $U_i^{\Delta x}$ with $i = 1, 2, \dots, N_x$ the cell average of the generic macroscopic quantity adopting a uniform discretization with respect to x of step size Δx . Halving the step size, the corresponding quantity is $U_i^{\Delta x/2}$ with $i = 1, 2, \dots, 2N_x$. Following [36], to compare the solutions on the two meshes, we adopt a similar approach employed for finite volumes schemes. We set

$$\tilde{U}_i^{\Delta x/2} = \frac{1}{2} \left[U_{2i-1}^{\Delta x/2} + U_{2i}^{\Delta x/2} \right], \quad i = 1, 2, \dots, N_x,$$

which is the cell average computed with the finer solution on the coarser mesh. We define the error as

$$\text{Err}_U^p(\Delta x) = \left\| U^{\Delta x} - \tilde{U}^{\Delta x/2} \right\|_p,$$

where $\|\cdot\|_p$ indicates the $L^p([0, L])$ norm. Consequently, the convergence rate α_U^p is

$$\alpha_U^p = \log_2 \left(\frac{\text{Err}_U^p(\Delta x)}{\text{Err}_U^p(\Delta x/2)} \right).$$

We summarize the obtained results in the Table 2. Even if a full second order is not reached, it is evident that in the adopted norms a convergence rate definitely higher than one is obtained.

Regarding the convergence of the scheme with respect to ε and θ we consider a fixed discretization with respect to x with $N_x = 40$ cells. Let $U_i^{\Delta \varepsilon}$ and $U_i^{\Delta \theta}$ with $i = 1, 2, \dots, N_x$ the cell average of the

generic macroscopic quantity adopting a uniform discretization with respect to ε and θ of step size $\Delta\varepsilon$ and $\Delta\theta$, respectively. The errors are defined as

$$\text{Err}_U^p(\Delta\varepsilon) = \left\| U^{\Delta\varepsilon} - U^{\Delta\varepsilon/2} \right\|_p \quad \text{and} \quad \text{Err}_U^p(\Delta\theta) = \left\| U^{\Delta\theta} - U^{\Delta\theta/2} \right\|_p.$$

Moreover, when the convergence study is done with respect to ε we consider a fixed discretization with respect to θ of $N_\theta = 32$ cells; when the convergence study is done with respect to θ we consider a fixed discretization with respect to ε of $N_\varepsilon = 40$ cells. The convergence results with respect to ε and θ are reported in Tables 3 and 4, respectively. The results are similar to those for spatial mesh but a bit worse, especially for the θ -mesh. In any case an order greater than one is obtained. The lesser accuracy in ε and θ presumably is to ascribe to the adoption of elements which are linear in x but constant with respect to other variables. Our choice represents a good compromise between accuracy and computational complexity.

U	N_x	Err_U^1	α_U^1	Err_U^2	α_U^2	Err_U^∞	α_U^∞
n	40	4.2677e-01		3.0449e+00		3.1555e+01	
	80	6.3712e-02	2.7435	5.2056e-01	2.5483	9.2600e+00	1.7688
	160	1.7837e-02	1.8367	1.4056e-01	1.8889	2.9350e+00	1.6577
	slope		2.2901		2.2186		1.7132
$V^{x,n}$	40	3.3900e-06		2.4872e-05		2.6115e-04	
	80	5.2712e-07	2.6851	4.1572e-06	2.5808	7.4100e-05	1.8173
	160	1.4269e-07	1.8853	1.1403e-06	1.8662	2.3800e-05	1.6385
	slope		2.2852		2.2235		1.7279
E^n	40	7.6050e-07		4.9671e-06		5.6150e-05	
	80	1.1925e-07	2.6730	7.0638e-07	2.8139	9.3000e-06	2.5940
	160	3.0312e-08	1.9760	1.8218e-07	1.9551	3.1500e-06	1.5619
	slope		2.3245		2.3845		2.0779

Table 2: Convergence rate with respect to x keeping fixed $N_\varepsilon = 80$ and $N_\theta = 32$.

U	N_x	Err_U^1	α_U^1	Err_U^2	α_U^2	Err_U^∞	α_U^∞
n	40	3.1633e+01		1.0448e+02		4.6315e+02	
	80	8.2431e+00	1.9402	2.7416e+01	1.9301	1.2676e+02	1.8694
	160	1.9766e+00	2.0602	6.5795e+00	2.0590	3.1370e+01	2.0146
	slope		2.0002		1.9946		1.9420
$V^{x,n}$	40	5.3858e-04		1.7839e-03		8.2872e-03	
	80	1.5670e-04	1.7811	5.1889e-04	1.7815	2.4323e-03	1.7686
	160	3.8789e-05	2.0143	1.2843e-06	2.0145	6.0800e-04	2.0146
	slope		1.8977		1.8980		1.8844
E^n	40	3.9385e-04		1.2562e-03		4.4673e-03	
	80	1.2016e-04	1.7127	3.8373e-04	1.7109	1.3848e-03	1.6897
	160	3.2771e-05	1.8745	1.0465e-04	1.8745	3.7820e-04	1.8725
	slope		1.7936		1.7927		1.7811

Table 3: Convergence rate with respect to ε keeping fixed $N_x = 40$ and $N_\theta = 32$.

In the sequel a numerical mesh of $N_x = 80$, $N_\varepsilon = 100$, and $N_\theta = 32$ cells is adopted. We apply an external electric field of before of 1 and then of 2 V/ μm . The stationary regime is reached in about 1 ps also for the electric field of 2 V/ μm .

In Fig. 6 we show the stationary electron density, current density, and mean energy. At the boundaries a jump in such quantities, represented by the dashed lines, along the metal-semiconductor junction is observed. This can be ascribed to the different states available in the contact, which is considered as a

U	N_x	Err_U^1	α_U^1	Err_U^2	α_U^2	Err_U^∞	α_U^∞
n	32	3.1998e+01		1.0712e+02		6.4936e+02	
	64	1.1621e+00	1.4612	3.8530e+01	1.4752	2.5946e+02	1.3235
	128	4.3586e+00	1.4148	1.4288e+01	1.4312	1.0544e+02	1.2991
	slope		1.4380		1.4532		1.3113
$V^{x,n}$	32	2.0632e-04		7.6983e-04		5.5621e-03	
	64	7.3795e-05	1.4833	2.7428e-04	1.4889	2.2769e-03	1.2886
	128	2.6938e-05	1.4539	9.8183e-05	1.4821	8.8980e-04	1.3555
	slope		1.4686		1.4855		1.3220
E^n	32	5.9165e-05		1.9778e-04		1.1366e-03	
	64	2.0734e-05	1.5127	6.8979e-05	1.5196	4.8840e-04	1.2186
	128	7.7378e-06	1.4220	2.5337e-05	1.4449	1.7300e-04	1.4973
	slope		1.4674		1.4822		1.3579

Table 4: Convergence rate with respect to ε keeping fixed $N_x = 40$ and $N_\varepsilon = 40$.

reservoir, and the graphene; in fact, we have an abrupt passage from a 3D material, the metal, and a 2D material, the graphene. The electron density presents a depletion area close to the source contacts and an accumulation region close to the drain contact. In steady state, the electron density is constant along the device length. The mean energy exhibits a qualitative behavior similar to the electron density.

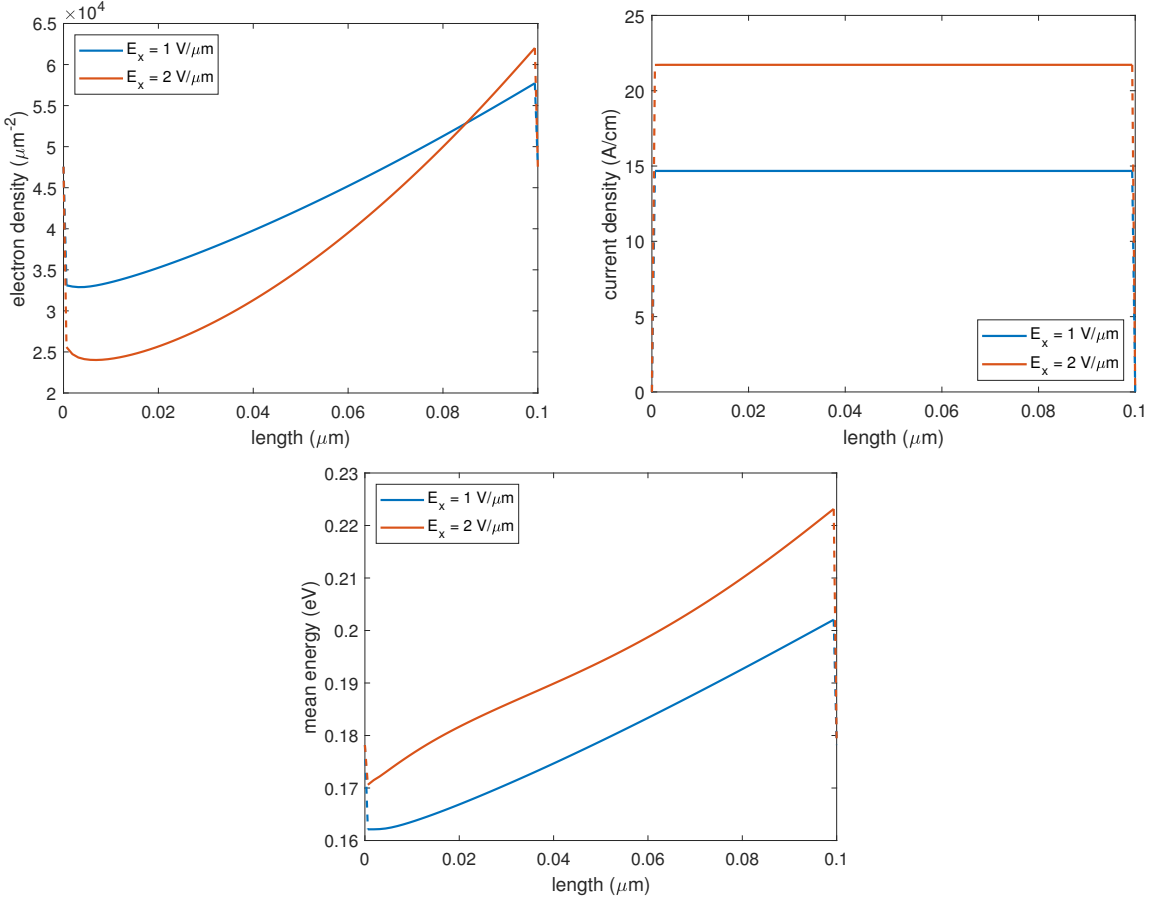


Figure 6: Stationary electron density (top-left), current density (top-right) and mean energy (bottom) of the device schematized in Fig. 1 for applied fields of $1 \text{ V}/\mu\text{m}$ and $2 \text{ V}/\mu\text{m}$.

In Figs. 7, 8 we show the stationary $a_{i,k,n}$ and $b_{i,k,n}$ coefficients of the approximated distribution

function (28). We observe that a second spike appears in the plot of the distribution function when the electric field is $2 \text{ V}/\mu\text{m}$ while is missing for $1 \text{ V}/\mu\text{m}$. It is clear that such an effect is due to the strength of the electric field which accentuates the anisotropy of the distribution function.

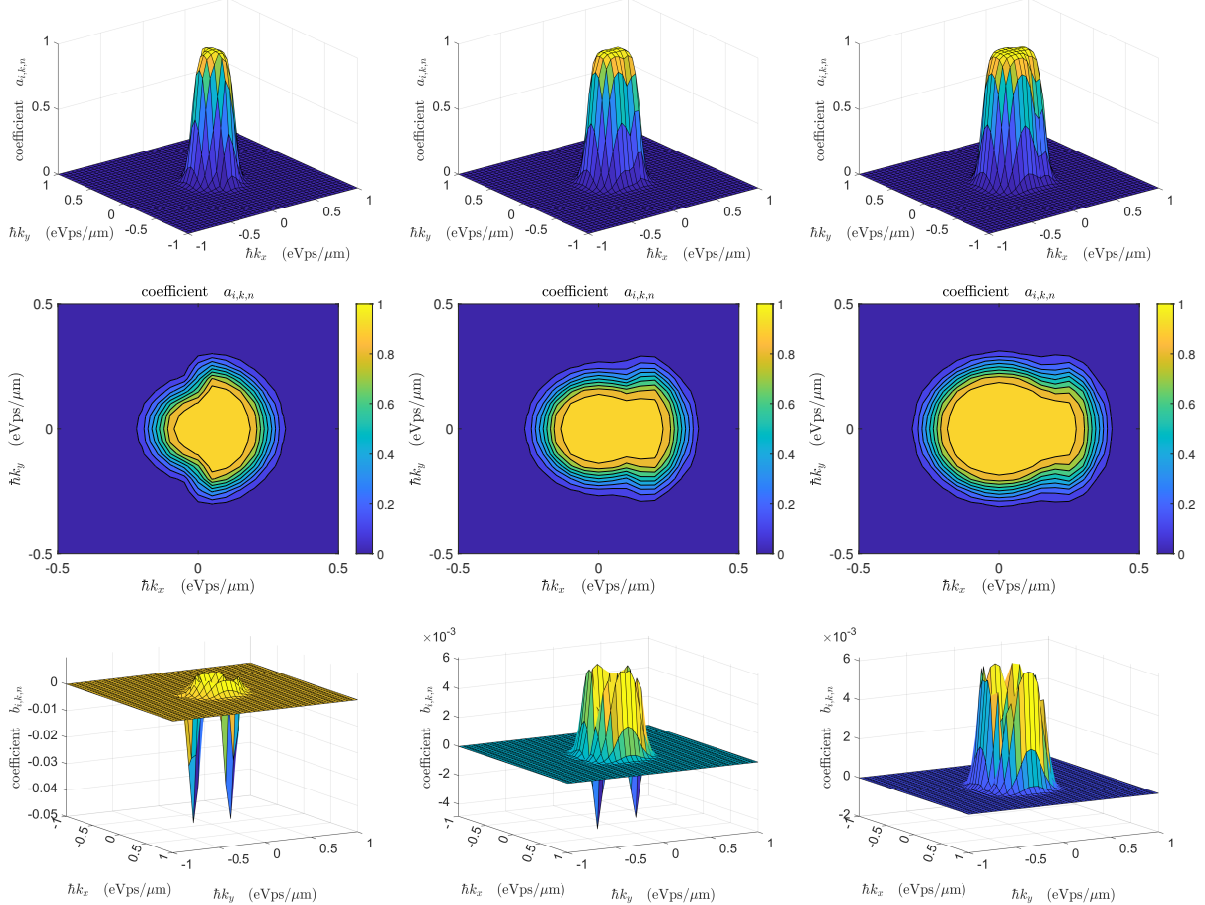


Figure 7: Stationary $a_{i,k,n}$ coefficient of the approximated distribution function (28) at $x = 0$ (top-left), $x = L/2$ (top-center) and $x = L$ (top-right) of the ideal device schematized in Fig. 1. Contour plot of the $a_{i,k,n}$ coefficient at the same positions (central line plots). Stationary $b_{i,k,n}$ coefficient of the approximated distribution function at $x = 0$ (bottom-left), $x = L/2$ (bottom-center) and $x = L$ (bottom-right). Applied field of $1 \text{ V}/\mu\text{m}$.

5.2 Test case 2: GFET

The second test case is the simulation of the charge transport in the GFET described in Sec. 3 and schematized in Fig. 2. For the simulations, we consider $L = 100 \text{ nm}$, $H = 21 \text{ nm}$, $V_G = 0.4 \text{ V}$, and $V_b = 0.1 \text{ V}$. We adopt a numerical mesh of $N_x = 80$, $N_\varepsilon = 100$, and $N_\theta = 32$ cells. For the Poisson equation we discretize the domain in 81×23 points. The stationary regime is reached in about 0.5 ps .

In Fig. 9 we show the stationary electron density, the current density and the mean energy versus position of the simulated GFET. The different lines refer to simulations performed with a distinct number of cells for the spatial discretization. Observe that the density presents a boundary layer close to the interface metal-graphene which is better resolved as the mesh is refined. The presence of such behavior can be explained with the same considerations of the test case 1. The current is constant in the interior of the domain. The linear shape close to the contacts tends to diminish as the mesh is refined. So, we can ascribe such an effect to the numerical approximation.

Finally, in Fig. 10 we present the stationary $a_{i,k,n}$ and $b_{i,k,n}$ coefficients of the approximated distribution function (28), referred to the simulated GFET while in Fig. 11 we show the stationary electrostatic potential, obtained solving the Poisson equation (3) on the 2D device section, and the stationary electric

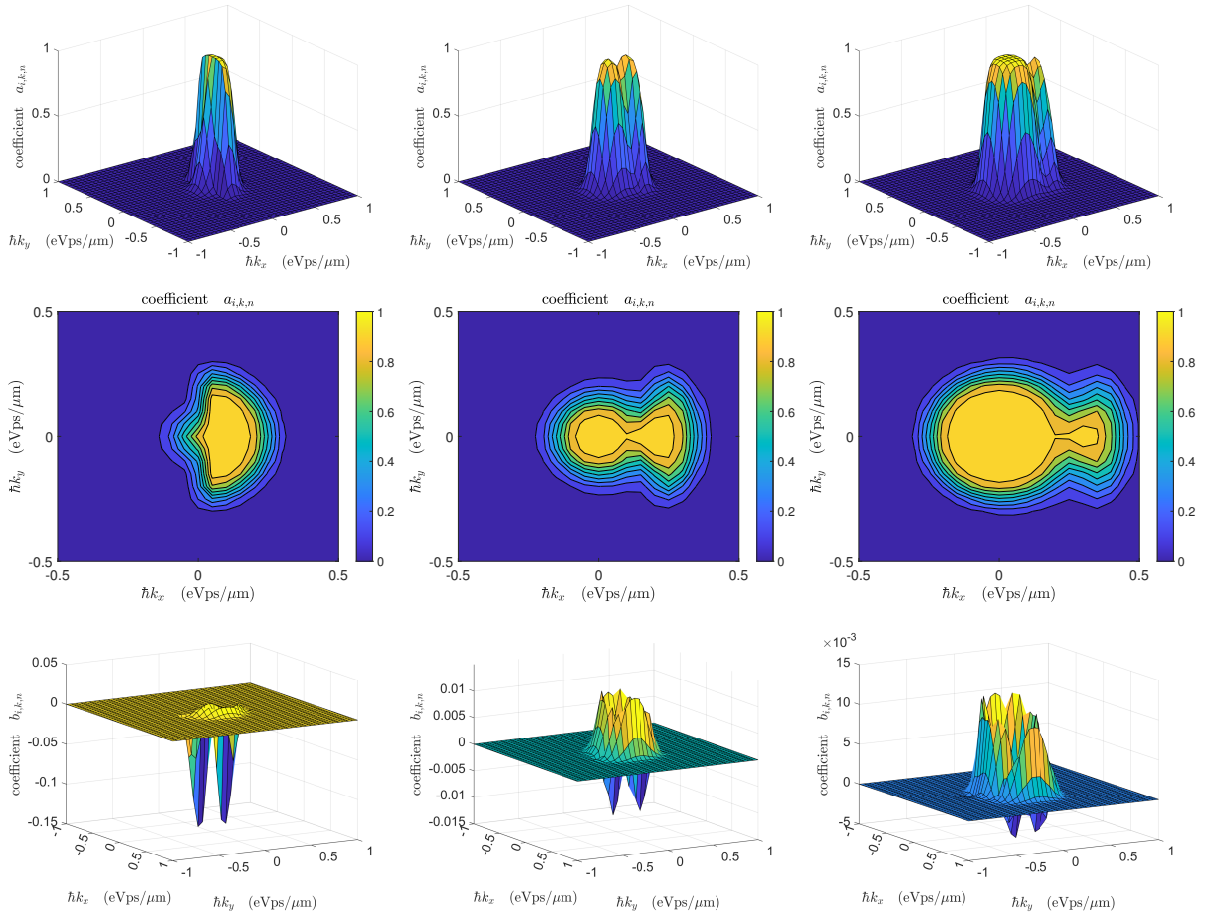


Figure 8: Stationary $a_{i,k,n}$ coefficient of the approximated distribution function (28) at $x = 0$ (top-left), $x = L/2$ (top-center) and $x = L$ (top-right) of the ideal device schematized in Fig. 1. Contour plot of the $a_{i,k,n}$ coefficient at the same positions (central line plots). Stationary $b_{i,k,n}$ coefficient of the approximated distribution function at $x = 0$ (bottom-left), $x = L/2$ (bottom-center) and $x = L$ (bottom-right). Applied field of 2 V/ μ m.

field computed along the graphene layer, i.e. along $y = y_{gr}$. As expected, the higher anisotropy of the distribution function is in the middle of the graphene layer.

6 Conclusions and acknowledgments

In this work, we have presented a numerical scheme for the numerical resolution of the Boltzmann transport equation in graphene field-effect transistors, employing a discontinuous Galerkin discretization with linear elements in the spatial coordinate and constant approximation for the wave-vector space, discretized with a polar mesh. In order to assure the correct physical range for the distribution function the maximum-principle-satisfying scheme introduced in [35] has been adopted.

The proposed method demonstrates very robust and possesses a good degree of accuracy, making it particularly well suited for capturing the complex charge transport dynamics inherent to graphene-based devices. By providing reliable and precise benchmark solutions, this approach enables a rigorous assessment of macroscopic models, such as drift-diffusion and hydrodynamic formulations. The combination of the DG method with linear spatial elements ensures computational efficiency while preserving the essential physical features of the system, establishing the framework as a valuable tool for both theoretical investigations and device-level simulations of graphene transistors.

The authors acknowledge the support from INdAM (GNFM) and from MUR progetto PRIN “Trans-

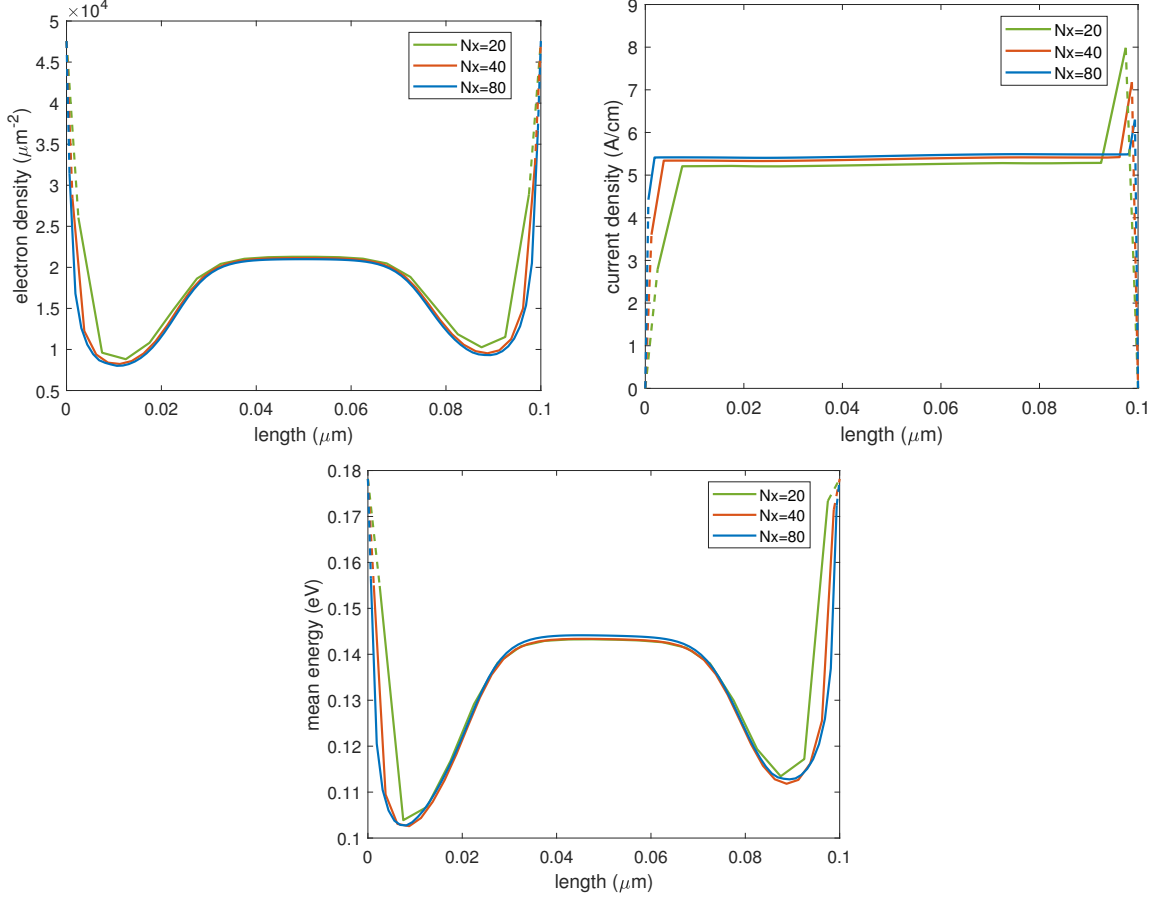


Figure 9: Stationary electron density (top-left), current density (top-right) and mean energy (bottom) of the simulated GFET of Fig. 2.

port phonema in low dimensional structures: models, simulations and theoretical aspects CUP E53D23005900006”.

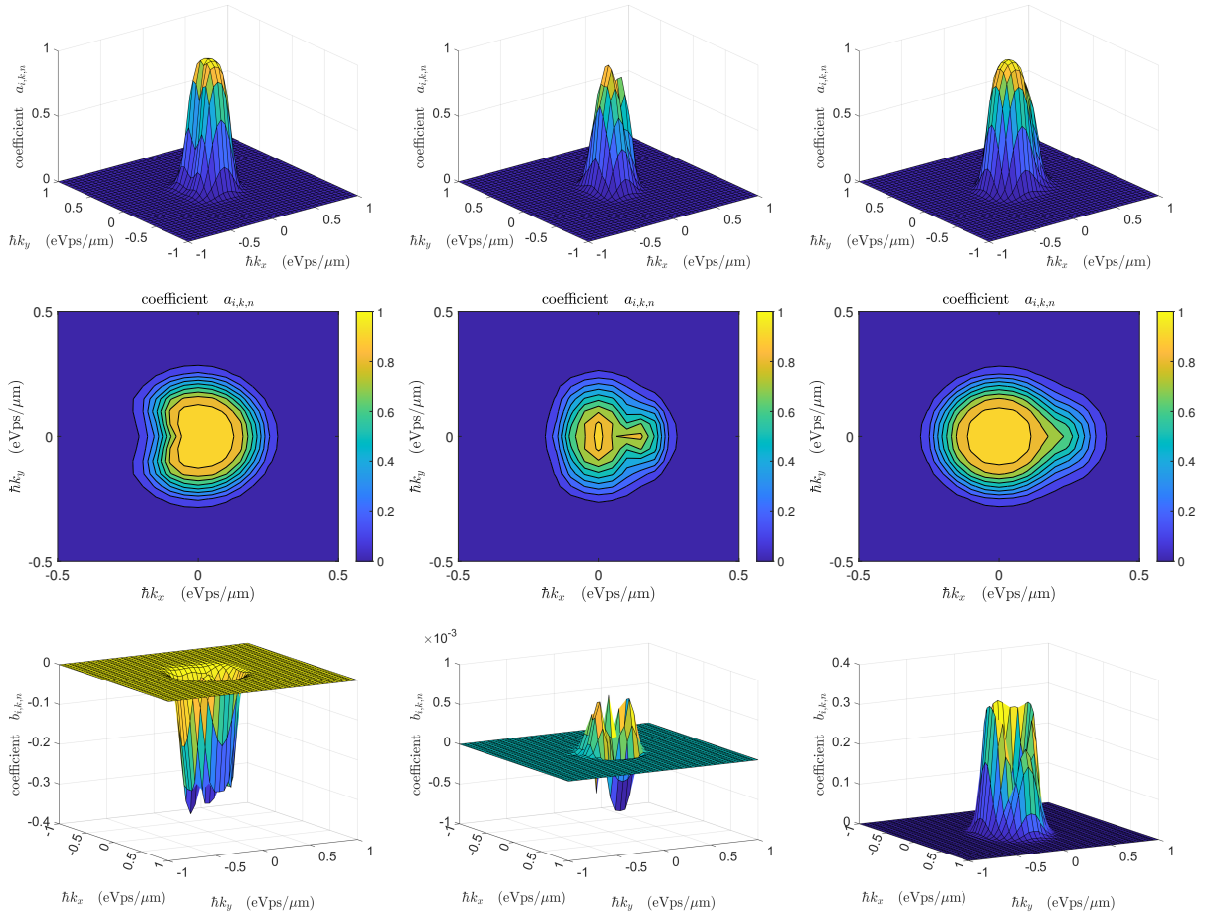


Figure 10: Stationary $a_{i,k,n}$ coefficient of the approximated distribution function (28) at $x = 0$ (top-left), $x = L/2$ (top-center) and $x = L$ (top-right) of the simulated GFET of Fig. 2. Contour plot of the $a_{i,k,n}$ coefficient at the same positions (central line plots). Stationary $b_{i,k,n}$ coefficient of the approximated distribution function at $x = 0$ (bottom-left), $x = L/2$ (bottom-center) and $x = L$ (bottom-right). Applied field of $1 \text{ V}/\mu\text{m}$.

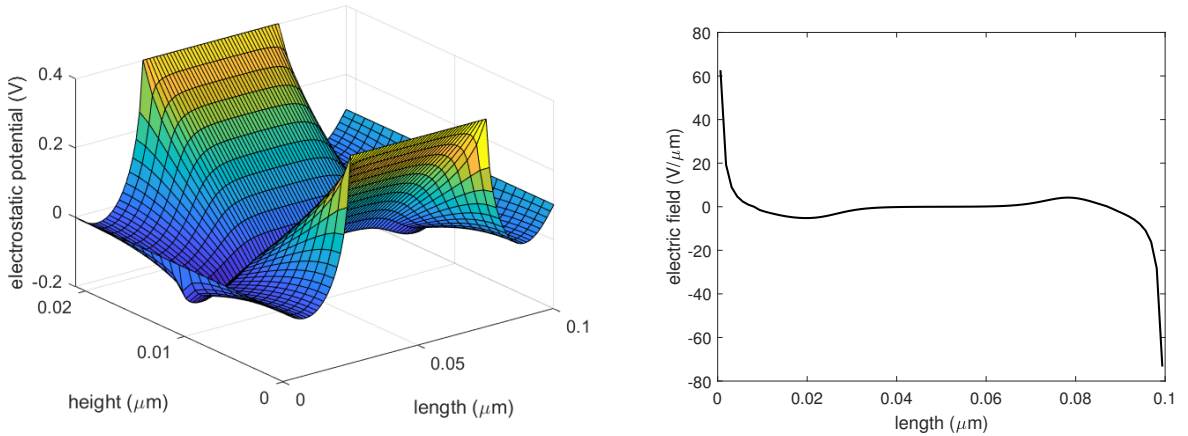


Figure 11: Stationary electrostatic potential (left) and stationary electric field along the graphene layer (right) of the simulated GFET of Fig. 2.

References

[1] A. H. Castro Neto, F. Guinea, N. M. R. Peres, K. S. Novoselov, A. K. Geim, The electronic properties of graphene, *Rev. Mod. Phys.*, 81, 109–162 (2009)

- [2] F. Schwierz, Graphene transistors, *Nat. Nanotechnol.*, 5, 487–496 (2010)
- [3] D. Jiménez, O. Moldovan, Explicit drain-current model of graphene field effect transistors targeting analog and radio-frequency applications, *IEEE Trans. Electron Devices*, 65, 739–746 (2018).
- [4] A.K. Upadhyay, A.K. Kushwaha, S.K. Vishvakarma, A unified scalable quasi-ballistic transport model of GFET for circuit simulations, *IEEE Trans. Electron Devices*, 58, 4049–4052 (2018).
- [5] G. Nastasi, V. Romano, A full coupled drift-diffusion-Poisson simulation of a GFET, *Commun. Nonlinear Sci. Numer. Simulat.*, 87, 105300 (2020).
- [6] C. Jourdana, P. Pietra, An interface formulation for the Poisson equation in the presence of a semiconducting single-layer materialm, *ESAIM: M2AN*, 58, 833–56 (2024).
- [7] L. Barletti, Hydrodynamic equations for electrons in graphene obtained from the maximum entropy principle, *J. Math. Phys.*, 55(8), 083303 (2014)
- [8] L. Barletti, Hydrodynamic equations for an electron gas in graphene, *J. Math. Industry*, 6:7 (2016)
- [9] L. Luca, V. Romano, Comparing linear and nonlinear hydrodynamical models for charge transport in graphene based on the maximum entropy principle, *Int. J. Non-linear Mech.*, 104, 39–58 (2018).
- [10] L. Luca, V. Romano, Quantum corrected hydrodynamic models for charge transport in graphene, *Ann. of Physics*, 406, 30-53 (2019)
- [11] V.D. Camiola, V. Romano, G. Vitanza, Quantum MEP Hydrodynamical Model for Charge Transport, *Journal of Statistical Physics*, 192, 20 (2025).
- [12] G. Mascali, V. Romano, A hierarchy of macroscopic models for phonon transport in graphene, *Physica A: Statistical Mechanics and its Applications*, 548, 124489 (2020).
- [13] B. Cockburn, C.-W. Shu, The Runge–Kutta Discontinuous Galerkin Method for Conservation Laws V: Multidimensional Systems, *Journal of Computational Physics*, Volume 141, Issue 2, Pages 199-224 (1998).
- [14] J.S. Hesthaven, T. Warburton, *Nodal Discontinuous Galerkin Methods*, Springer New York, NY (2008)
- [15] Y. Cheng, I. M. Gamba, A. Majorana, C.-W. Shu, A discontinuous Galerkin solver for Boltzmann-Poisson systems in nano devices, *Comput. Methods Appl. Mech. Engrg.*, 198(37-40), 3130–3150 (2009)
- [16] Y. Cheng, I. M. Gamba, A. Majorana, C.-W. Shu, A brief survey of the discontinuous Galerkin method for the Boltzmann-Poisson equations, *Boletin de la Sociedad Espanola de Matematica Aplicada*, 54, 47–64 (2011)
- [17] A. Majorana, G. Nastasi, V. Romano, Simulation of Bipolar Charge Transport in Graphene by Using a Discontinuous Galerkin Method, *Comm. Comp. Phys.*, 26(1), 114–134 (2019)
- [18] G. Nastasi, V. Romano, Discontinuous Galerkin approach for the simulation of charge transport in graphene, *Ricerche di Matematica*, 70, 149–165 (2021).
- [19] P. Lichtenberger, O. Morandi, F. Schürer, High-field transport and optical phonon scattering in graphene, *Phys. Rev. B*, 84, 045406 (2011)
- [20] G. Nastasi, V. Romano, An Efficient GFET Structure, *IEEE Trans. Electron Devices*, 68(9), 4729–4734 (2021)
- [21] C. Jacoboni, *Theory of Electron Transport in Semiconductors*, Springer-Verlag (2013)
- [22] E. H. Hwang, S. Adam, S. Das Sarma, Carrier Transport in Two-Dimensional Graphene Layers, *Phys. Rev. Lett.*, vol. 98, no. 18, 186806 (2007)
- [23] S. Das Sarma, S. Adam, E. H. Hwang, E. Rossi, Electronic transport in two-dimensional graphene, *Rev. Mod. Phys.*, vol. 83, No. 2, 407–470 (2011)

- [24] H. Hirai, H. Tsuchiya, Y. Kamakura, N. Mori, M. Ogawa, Electron mobility calculation for graphene on substrates, *Journal of Applied Physics*, vol. 116, 083703 (2014)
- [25] M. Coco, A. Majorana, V. Romano, Cross validation of discontinuous Galerkin method and Monte Carlo simulations of charge transport in graphene on substrate, *Ricerche mat.*, 66, 201–220 (2017)
- [26] M. Coco, A. Majorana, G. Nastasi, V. Romano, High-field mobility in graphene on substrate with a proper inclusion of the Pauli exclusion principle, *Atti Accad. Pelorit. Pericol. Cl. Sci. Fis. Mat. Nat.*, 97(S1), A6 (2019)
- [27] F. Mustieles, Global existence of solutions for the nonlinear Boltzmann equation of semiconductor physics, *Rev. Mat. Iberoam.*, 6, 43–59 (1990).
- [28] J. H. Chang, A. Huzayyin, K. Lian, F. Dawson, Quantum capacitance of graphene in contact with metal, *Appl. Phys. Lett.*, 107(19), 193902 (2015).
- [29] O. Frank, J. Vejpravova, V. Holy, L. Kavan, M. Kalbac, Interaction between graphene and copper substrate: The role of lattice orientation, *Carbon*, 68, 440–451 (2014).
- [30] A.L. Walter, S. Nie, A. Bostwick, K.S. Kim, L. Moreschini, Y.J. Chang, D. Innocenti, K. Horn, K.F. McCarty, E. Rotenberg, Electronic structure of graphene on single-crystal copper substrates, *Phys. Rev. B*, 84(19), 195443(2011).
- [31] A. Harten, S. Osher, Uniformly High-Order Accurate Nonoscillatory Schemes. I, *SIAM Journal on Numerical Analysis*, 24(2), 279–309 (1987)
- [32] G. Nastasi, V.D. Camiola, V. Romano, Direct Simulation of Charge Transport in Graphene Nanoribbons, *Commun. Comput. Phys.*, 31(2), 449–494 (2022)
- [33] C.-W. Shu, S. Osher, Efficient implementation of essentially non-oscillatory shock-capturing schemes, *Journal of Computational Physics*, 77(2), 439–471 (1988)
- [34] G. Nastasi, A. Borzì, V. Romano, Optimal control of a semiclassical Boltzmann equation for charge transport in graphene, *Communications in Nonlinear Science and Numerical Simulation*, 132, 107933 (2024)
- [35] X. Zhang, C.-W. Shu, On maximum-principle-satisfying high order schemes for scalar conservation laws, *Journal of Computational Physics*, 229, 3091–3120 (2010)
- [36] E. Toro, *Riemann Solvers and Numerical Methods for Fluid Dynamics*, Springer Berlin, Heidelberg, 2009.